

1 Non-Hydrostatic RegCM4 (RegCM4-NH): Model description and  
2 case studies over multiple domains.

3 Coppola Erika (1), Stocchi Paolo (2), Pichelli Emanuela (1), Torres Alavez Jose Abraham  
4 (1), Glazer Russel (1), Giuliani Graziano (1), Di Sante Fabio (1), Nogherotto Rita (1),  
5 Giorgi Filippo (1)

6

7 *Correspondence to:* Erika Coppola ([coppolae@ictp.it](mailto:coppolae@ictp.it))

8 1. International Centre for Theoretical Physics (ICTP), Trieste, Italy  
9 2. Institute of Atmospheric Sciences and Climate, National Research Council of Italy,  
10 CNR-ISAC, Bologna, Italy

11 **Abstract.** We describe the development of a non-hydrostatic version of the regional  
12 climate model RegCM4, called RegCM4-NH, for use at convection-permitting resolutions.  
13 The non-hydrostatic dynamical core of the Mesoscale Model MM5 is introduced in the  
14 RegCM4, with some modifications to increase stability and applicability of the model to  
15 long-term climate simulations. Newly available explicit microphysics schemes are also  
16 described, and three case studies of intense convection events are carried out in order to  
17 illustrate the performance of the model. They are all run at convection-permitting grid  
18 spacing of 3 km over domains in northern California, Texas and the Lake Victoria region,  
19 without the use of parameterized cumulus convection. A substantial improvement is found  
20 in several aspects of the simulations compared to corresponding coarser resolution (12  
21 km) runs completed with the hydrostatic version of the model employing parameterized  
22 convection. RegCM4-NH is currently being used in different projects for regional climate  
23 simulations at convection-permitting resolutions, and is intended to be a resource for  
24 users of the RegCM modeling system.

25

26 **Keywords**

27 Regional climate models; RegCM4; km-scale resolution; climate change

28 **Introduction**

29 Since the pioneering work of Dickinson et al. (1989) and Giorgi and Bates (1989),  
30 documenting the first regional climate modeling system (RegCM, version 1) in literature,  
31 the dynamical downscaling technique based on limited area Regional Climate Models  
32 (RCMs) has been widely used worldwide, and a number of RCM systems have been  
33 developed (Giorgi 2019). RegCM1 (Dickinson et al., 1989, Giorgi and Bates, 1989) was  
34 originally developed at the National Center for Atmospheric Research (NCAR) based on  
35 the Mesoscale Model version 4 (MM4) (Anthes et al, 1987) . Then, further model versions  
36 followed: RegCM2 (Giorgi et al. 1993a,b), RegCM2.5, (Giorgi and Mearns 1999),  
37 RegCM3 (Pal et al. 2007), and lastly RegCM4 (Giorgi et al 2012). Except for the transition  
38 from RegCM1 to RegCM2, in which the model dynamical core was updated from that of  
39 the MM4 to that of the MM5 (Grell et al. 1995), these model evolutions were mostly based  
40 on additions of new and more advanced physics packages. RegCM4 is today used by a  
41 large community for numerous projects and applications, from process studies to paleo  
42 and future climate projections, including participation in the Coordinated Regional  
43 Downscaling EXperiment (CORDEX, Giorgi et al. 2009; Gutowski et al. 2016). The model  
44 can also be coupled with ocean, land and chemistry/aerosol modules in a fully interactive  
45 way (Sitz et al. 2017).

46 The dynamical core of the standard version of RegCM4 is hydrostatic, with sigma-p  
47 vertical coordinates. As a result, the model can be effectively run for grid spacings of ~10  
48 km or larger, for which the hydrostatic assumption is valid. However, the RCM community  
49 is rapidly moving to higher resolutions of a few km, i.e. “convection-permitting” (Prein et  
50 al. 2015; Coppola et al. 2020) and therefore the dynamical core of RegCM4 has been  
51 upgraded to include a non-hydrostatic dynamics representation usable for very high  
52 resolution applications. This upgrade, which we name RegCM4-NH, is essentially based  
53 on the implementation of the MM5 non-hydrostatic dynamical core within the RegCM4  
54 framework, which has an entirely different set of sub-grid model physics compared to  
55 MM5.

56

57 RegCM4-NH is already being used in some international projects focusing on climate  
58 simulations at convection-permitting km-scales, namely the European Climate Prediction

59 System (EUCP, Hewitt and Lowe 2018) and the CORDEX Flagship Pilot Study dedicated  
60 to convection (CORDEX-FPSCONV, Coppola et al. 2020), and it is starting to be used  
61 more broadly by the RegCM modeling community.

62 For example, the recent papers by Ban et al. (2021) and Pichelli et al. (2021) document  
63 results of the first multi-model experiment of 10-year simulations at the convection-  
64 permitting scales over the so-called greater Alpine region. Two different simulations with  
65 RegCM4-NH for present day conditions have contributed to the evaluation analysis of  
66 Ban et al. (2021). They were carried out at the International Centre for Theoretical Physics  
67 (ICTP) and the Croatian Meteorological and Hydrological Service (DHMZ) using two  
68 different physics configurations. The results show that RegCM4-NH largely improves the  
69 precipitation simulation as compared to available fine scale observations when going from  
70 coarse to high resolution, in particular for higher order statistics, such as precipitation  
71 extremes and hourly intensity. Pichelli et al. (2021) then analyse multi-model ensemble  
72 simulations driven by selected CMIP5 GCM projections for the decades 1996–2005 and  
73 2090–2099 under the RCP8.5 scenario. ICTP contributed to the experiment with  
74 simulations using RegCM4-NH driven by the MOCH-HadGEM GCM (r1i1p1) in a two  
75 level nest configuration (respectively at 12 and 3 km grid). The paper shows new insights  
76 into future changes, for example an enhancement of summer and autumn hourly rainfall  
77 intensification compared to coarser resolution model experiments, as well as an increase  
78 of frequency and intensity of high-impact weather events.

79

80 In this paper we describe the structure of RegCM4-NH and provide some illustrative  
81 examples of its performance, so that model users can have a basic reference providing  
82 them with background information on the model. In the next section we first describe the  
83 new model dynamical core, while the illustrative applications are presented in section 4.  
84 Section 5 finally provides some discussion of future developments planned for the RegCM  
85 system.

86

87 **Model description**

88 In the development of RegCM4-NH, the RegCM4 as described by Giorgi et al. (2012) was  
89 modified to include, the non-hydrostatic dynamical core (*idynamic* = 2 namelist option as  
90 described in RegCM-4.7.1/Doc/README.namelist of the source code) of the mesoscale  
91 model MM5 (Grell et al. 1995). This dynamical core was selected because RegCM4  
92 already has the same grid and variable structure as MM5 in its hydrostatic core, which  
93 substantially facilitated its implementation (Elguindi et al. 2017).

94

95 The model equations with complete description of the Coriolis force and a top radiative  
96 boundary condition, along with the finite differencing scheme, are given in Grell et al.  
97 (1995). Pressure,  $p$ , temperature,  $T$ , and density,  $\rho$ , are first decomposed into a  
98 prescribed reference vertical profile plus a time varying perturbation. The prognostic  
99 equations are then calculated using the pressure perturbation values. Compared to the  
100 original MM5 dynamical core, the following modifications were implemented in order to  
101 achieve increased stability for long term climate simulations (Elguindi et al. 2017  
102 document any modifications which follow the choice of the non-hydrostatic dynamical  
103 core through the namelist parameter *idynamic* = 2; further available user-dependant  
104 options, and the corresponding section in the namelist, are explicitly indicated):

105

106 i) The reference state temperature profile is computed using a latitude dependent  
107 climatological temperature distribution and thus is a function of the specific domain  
108 coordinates (*base\_state\_pressure*, *logp\_lrate* parameters in *&referenceatm*) (Elguindi et  
109 al. 2017). These two parameters were hard-coded in the original MM5 while for the  
110 RegCM are user configurable;

111

112 ii) The lateral time dependent boundary conditions (*iboudy* in *&physicsparam*) for each  
113 prognostic variable use the same exponential relaxation technique (*iboudy* = 5) described  
114 in Giorgi et al. (1993). The linear MM5 relaxation scheme is also kept as an option (*iboudy*  
115 = 1);

116

117    iii) The advection term in the model equations, which in the MM5 code is implemented  
 118    using a centered finite difference approach, was changed to include a greater upstream  
 119    weight factor as a function of the local Courant number (Elguindi et al. 2017). The  
 120    maximum value of the weight factor is user configurable (*uoffc* in *&dynparam*). As detailed  
 121    in the MM5 model description (Grell et al, 1995), the horizontal advection term for a scalar  
 122    variable *X* contributes to the total tendency as:

123

124    
$$\Delta_{adv} (p^* X)_G = -m^2|_G \left[ \frac{(p^* X|_{b/m}|_b - p^* X|_{a/m}|_a)}{dx} + \frac{(p^* X|_{d/m}|_d - p^* X|_{c/m}|_c)}{dy} \right]$$

125

126    where the *m* is the projection mapping factor and, with respect to Figure 1, assuming that  
 127    the computation is to be performed for the gold cross point *G*, the averages are performed  
 128    in the points *a, b, c, d*. For the *u/m* and *v/m* terms, the average value is computed using  
 129    respectively the values in points *AC, BD, CD, AB*.

130    In RegCM4 for the term *p<sup>\*</sup>X*, the model computes a weighted average value of the field  
 131    using the value in gold+cyan and gold+green cross points with weights increasing the  
 132    relative contribution of the upstream point up as a function of the local courant number:

133

134    
$$p^* X|_a = 0.5((1 - f_1)p^* X|_G + (1 + f_1)p^* X|_{c_1})$$

135    
$$p^* X|_b = 0.5((1 - f_1)p^* X|_{c_2} + (1 + f_1)p^* X|_G)$$

136    
$$p^* X|_c = 0.5((1 - f_2)p^* X|_G + (1 + f_2)p^* X|_{g_1})$$

137    
$$p^* X|_d = 0.5((1 - f_2)p^* X|_{g_2} + (1 + f_2)p^* X|_G)$$

138    where *f<sub>1</sub>, f<sub>2</sub>* are defined as the local Courant number for the 1D advection equations  
 139    multiplied for a control factor:

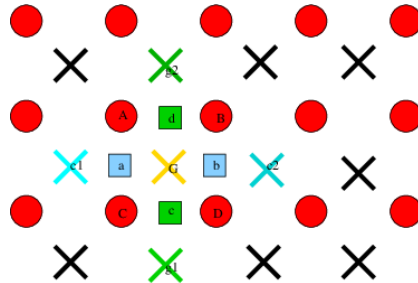
140

141    
$$f_1 = \mu_{fc} dt \frac{(u|_a + u|_b)}{2dx}$$

142    
$$f_2 = \mu_{fc} dt \frac{(v|_c + v|_d)}{2dy};$$

143

144



145

146 **Figure 1 Schematic representation showing the horizontal advection scheme**  
 147 **staggering. Circles are U,V points. X are scalar variable points.**

148

149

150 iv) The water species (cloud, ice, rain, snow) term uses the same advection scheme as  
 151 the other variables (Elguindi et al. 2017) and not a complete upstream scheme as in the  
 152 MM5 code (Grell et al. 1995);

153

154 v) A local flux limiter reduces the advection terms in order to remove unrealistic strong  
 155 gradients and its limits are user configurable (in the *&dynparam* section the maximum  
 156 gradient fraction for advection: temperature, *t\_extrema*, specific humidity, *q\_rel\_extrema*,  
 157 liquid cloud content, *c\_rel\_extrema* and for tracers, *t\_rel\_extrema*). This was hardcoded  
 158 in the MM5 code and the limits were not user configurable;

159

160 vi) The diffusion stencil of the Laplace equation uses a nine point approach as in LeVeque  
 161 (2006) and a topography dependent environmental diffusion coefficient is added to  
 162 reduce spurious diffusion along pressure coordinate slopes (Elguindi et al. 2017) as in  
 163 the hydrostatic version of the code (Giorgi et al. 1993b). The change in stencil does not  
 164 affect the overall fourth order precision of the model, but reduces the computational  
 165 stencil size, thus reducing the communication overhead;

166

167 vii) The top boundary radiative condition (*ifupr* = 1 in *&nonhydparam*) adopted in the  
 168 semi-implicit vertical differencing scheme to reduce the reflection of energy waves uses  
 169 coefficients on a 13x13 matrix which are re-computed every simulation day and not kept

170 constant throughout the whole simulation as in the MM5 code. This allows the model to  
171 be run for longer simulation times while not being strongly tied to the initial atmospheric  
172 conditions;

173

174 viii) The dynamical control parameter  $\beta$  in the semi-implicit vertical differencing scheme  
175 (*nhbet* in *&nonhydromodel*) used for acoustic wave damping (Elguindi et al. 2017) is user  
176 configurable (Klemp and Dudhia, 2008), while it is hard-coded in the MM5;

177

178 ix) A Rayleigh damping (*ifrayd* = 1 in *&nonhydromodel*) of the status variables towards  
179 the input GCM boundary conditions can be activated in the top layers (*rayndamp*  
180 configuring the number of top levels to apply) with a configurable relaxation time  
181 (*rayalpha0*, Klemp and Lilly, 1978, Durran and Klemp, 1983. This is consistent to what is  
182 implemented in the WRF model);

183

184 x) The water species time filtering uses the Williams (2009) modified filter with  $\alpha = 0.53$   
185 instead of the RA filter used by all the other variables. The  $\nu$  factor in the RA filter is user  
186 configurable (*gnu1* and *gnu2* in *&dynparam*). This reduces the damping introduced by the  
187 Robert-Asselin filter and the computational diffusion introduced by the horizontal  
188 advection scheme.

189

190 With these modifications, the model basic equations, under leap-frog integration scheme,  
191 are (Elguindi et al. 2017) :

192

193

$$\frac{\partial p^* u}{\partial t} = -m^2 \left[ \frac{\partial p^* uu/m}{\partial x} + \frac{\partial p^* vu/m}{\partial y} \right] - \frac{\partial p^* u \dot{\sigma}}{\partial \sigma} + u DIV - \frac{mp^*}{\rho} \left[ \frac{\partial p'}{\partial x} - \frac{\sigma}{p^*} \frac{\partial p^*}{\partial x} \frac{\partial p'}{\partial \sigma} \right] + p^* fv - p^* ew \cos \theta + D_u \quad (1)$$

194

195

196 
$$\frac{\partial p^* v}{\partial t} = -m^2 \left[ \frac{\partial p^* u v / m}{\partial x} + \frac{\partial p^* v v / m}{\partial y} \right] - \frac{\partial p^* v \dot{\sigma}}{\partial \sigma} + v DIV -$$

$$\frac{m p^*}{\rho} \left[ \frac{\partial p'}{\partial y} - \frac{\sigma}{p^*} \frac{\partial p^*}{\partial y} \frac{\partial p'}{\partial \sigma} \right] - p^* f u + p^* e w \sin \theta + D_v \quad (2)$$

197 
$$\frac{\partial p^* w}{\partial t} = -m^2 \left[ \frac{\partial p^* u w / m}{\partial x} + \frac{\partial p^* v w / m}{\partial y} \right] - \frac{\partial p^* w \dot{\sigma}}{\partial \sigma} + w DIV +$$

$$p^* g \frac{\rho_0}{\rho} \left[ \frac{1}{p^*} \frac{\partial p'}{\partial \sigma} + \frac{T'_v}{T} - \frac{T_0 p'}{T p_0} \right] - p^* g [(q_c + q_r)] + p^* e (u \cos \theta - v \sin \theta) + D_w \quad (3)$$

198 
$$\frac{\partial p^* p'}{\partial t} = -m^2 \left[ \frac{\partial p^* u p' / m}{\partial x} + \frac{\partial p^* v p' / m}{\partial y} \right] - \frac{\partial p^* p' \dot{\sigma}}{\partial \sigma} + p' DIV -$$

$$m^2 p^* \gamma p \left[ \frac{\partial u / m}{\partial x} - \frac{\sigma}{m p^*} \frac{\partial p^*}{\partial x} \frac{\partial u}{\partial \sigma} + \frac{\partial v / m}{\partial y} - \frac{\sigma}{m p^*} \frac{\partial p^*}{\partial y} \frac{\partial v}{\partial \sigma} \right] + \rho_0 g \gamma p \frac{\partial w}{\partial \sigma} + p^* \rho_0 g \quad (4)$$

199 
$$\frac{\partial p^* T}{\partial t} = -m^2 \left[ \frac{\partial p^* u T / m}{\partial x} + \frac{\partial p^* v T / m}{\partial y} \right] - \frac{\partial p^* T \dot{\sigma}}{\partial \sigma} + T DIV +$$

$$\frac{1}{\rho c_p} \left[ p^* \frac{D p'}{D t} - \rho_0 g p^* w - D_{p'} \right] + p^* \frac{\dot{Q}}{c_p} + D_T \quad (5)$$

200  
201 Where:

202 
$$DIV = m^2 \left[ \frac{\partial p^* u / m}{\partial x} + \frac{\partial p^* v / m}{\partial y} \right] + \frac{\partial p^* \dot{\sigma}}{\partial \sigma}$$

$$\dot{\sigma} = -\frac{\rho_0 g}{p^*} w - \frac{m \sigma}{p^*} \frac{\partial p^*}{\partial x} u - \frac{m \sigma}{p^*} \frac{\partial p^*}{\partial y} v$$

$$\tan \theta = -\cos \phi \frac{\partial \lambda / \partial y}{\partial \phi / \partial x}$$

203 
$$p(x, y, z, t) = p_0(z) + p'(x, y, z, t)$$

$$T(x, y, z, t) = T_0(z) + T'(x, y, z, t)$$

$$\rho(x, y, z, t) = \rho_0(z) + \rho'(x, y, z, t)$$

204 with the vertical sigma coordinate defined as:

205

206  
207  
208  
209  
210  
211

$$212 \quad \sigma = \frac{(p_0 - p_t)}{(p_s - p_t)}$$

$$213$$

$$214 \quad p_s \text{ is the surface pressure and } p_0 \text{ is the reference pressure profile. The total pressure}$$

$$215 \quad \text{at each grid point is thus given as:}$$

$$216$$

$$217 \quad p(x, y, z, t) = p^* \sigma(k) + p_t + p'(x, y, z, t)$$

$$218$$

$$219 \quad \text{With } p_t \text{ being the top model pressure assuming a fixed rigid lid.}$$

$$220 \quad \text{The model physics schemes for boundary layer, radiative transfer, land and ocean}$$

$$221 \quad \text{surface processes, cloud and precipitation processes are extensively described in Giorgi}$$

$$222 \quad \text{et al. (2012) and summarized in Table 1. For each physics component a number of}$$

$$223 \quad \text{parameterization options are available (Table 1), and can be selected using a switch}$$

$$224 \quad \text{selected by the user. As mentioned, the use of non-hydrostatic dynamics is especially}$$

$$225 \quad \text{important when going to convection-permitting resolutions of a few km (Prein et al. 2015).}$$

$$226 \quad \text{At these resolutions the scale separation assumption underlying the use of cumulus}$$

$$227 \quad \text{convection schemes is not valid any more, and explicit cloud microphysics}$$

$$228 \quad \text{representations are necessary. The RegCM4 currently includes two newly implemented}$$

$$229 \quad \text{microphysics schemes, the Nogherotto-Tompkins (Nogherotto et al. 2016) and the WSM5}$$

$$230 \quad \text{scheme from the Weather Research Forecast (WRF, Skamarok et al. 2008) model, which}$$

$$231 \quad \text{are briefly described in the next sections for information to model users.}$$

$$232$$

Model physics (Namelist flag)	Options	n. option	Reference
<b>Dynamical core</b> (idynamic)	Hydrostatic	1	Giorgi et al. 1993a,b Giorgi et al. 2012
	Non-Hydrostatic (*)	2	present paper
<b>Radiation</b>	CCSM	0	Kiehl et al. 1996

(irrtm)	RRTM (*)	1	Mlawer et al. 1997
<b>Microphysics</b> ( <i>ipptls</i> )	Subex	1	Pal et al 2000
	Nogherotto Thompson	2	Nogherotto et al. 2016
	WSM5 (*)	3	Hong et al 2004
<b>Cumulus</b> ( <i>icup</i> )	Kuo	1	Anthes et al. 1987
	Grell	2	Grell 1993
	Emanuel	4	Emanuel 1991
	Tiedtke	5	Tiedtke 1989, 1993
	Kain-Fritsch	6	Kain and Fritsch, 1990; Kain 2004
	MM5 Shallow cumulus (only mixing) (*)	-1	Grell et al. 1994
<b>Planetary Boundary Layer</b> ( <i>ibltyp</i> )	Modified-Holtslag	1	Holtslag et al., 1990
	UW	2	Bretherton et al. 2004
<b>Land Surface</b> (code compiling option)	BATS	/	Dickinson et al. 1993; Giorgi et al. 2003
	CLM4.5	/	Oleson et al. 2013
<b>Ocean Fluxes</b> ( <i>iocnflux</i> )	BATS	1	Dickinson et al. 1993
	Zeng	2	Zeng et al. 1998

	COARE	3	Fairall et al. 1996a,b
<b>Interactive lake</b> ( <i>lakemod</i> )	1D diffusion/convection	1	Hostetler et al. 1993
<b>Tropical band</b> ( <i>i_band</i> )	RegT-Band	1	Coppola et al. 2012
<b>Coupled ocean</b> ( <i>iocncpl</i> )	RegCM-ES	1	Sitz et al. 2017

233 **Table 1 Core and sub-grid physics scheme available in RegCM-NH. New schemes  
234 available with this release are starred (\*).**

235

236

237 **Explicit microphysics schemes**

238 ***Nogherotto-Tompkins Scheme***

239 A new parameterization for explicit cloud microphysics and precipitation built upon the  
240 European Centre for Medium Weather Forecast's Integrated Forecast System (IFS)  
241 module (Tiedtke [1993], Tompkins [2007]), was introduced in RegCM4 (*ipptls* = 2 in  
242 *&microparam*) by Nogherotto et al. [2016]. In the present configuration, the scheme  
243 implicitly solves 5 prognostic equations for water vapor, *qv*, cloud liquid water, *ql*, rain, *qr*,  
244 cloud ice, *qi*, and snow, *qs*, but it is also easily extendable to a larger number of variables.  
245 Water vapor, cloud liquid water, rain, cloud ice and snow are all expressed in terms of the  
246 grid-mean mixing ratio.

247 Cloud liquid and ice water content are independent, allowing the existence of supercooled  
248 liquid water and mixed-phase clouds. Rain and snow precipitate with a fixed terminal fall  
249 speed and can then be advected by the three dimensional winds. A check for the  
250 conservation of enthalpy and of total moisture is ensured at the end of each timestep. The  
251 governing equation for each variable is:

252

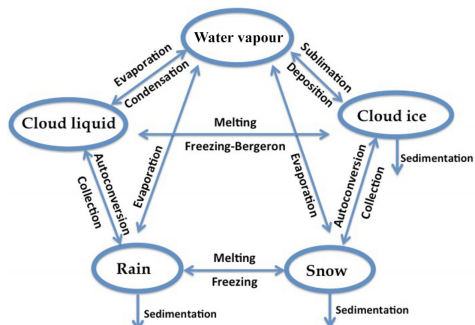
253

$$\frac{\partial q_x}{\partial t} = S_x + \frac{1}{\rho} \frac{\partial}{\partial z} (\rho V_x q_x)$$

254

255 The local variation of the mixing ratio  $q_x$  of the variable  $x$  is given by the sum of  
 256  $S_x$ , containing the net sources and sinks of  $q_x$  through microphysical processes (i.e.  
 257 condensation, evaporation, auto-conversion, melting, etc.), and the sedimentation term,  
 258 which is a function of the fall speed  $V_x$ . An upstream approach is employed to solve the  
 259 equations. The sources and sinks contributors are divided in two groups according to the  
 260 duration of the process they describe: processes that are considered to be fast relative to  
 261 the model time step are treated implicitly while slow processes are treated explicitly. The  
 262 processes taken into account (shown in Figure 2) are the microphysical pathways across  
 263 the 5 water variables: condensation, autoconversion, evaporation, cloud water collection  
 264 (accretion), and autoconversion for warm clouds, and freezing, melting, deposition,  
 265 sublimation for cold clouds.

266



268 **Figure 2: Depiction of the new scheme, showing the five prognostic variables and**  
 269 **how they are related to each other through microphysical processes**

270 For each microphysical pathway, phase changes are associated with the release or  
 271 absorption of latent heat, which then impacts the temperature budget. The impact is

272 calculated using the conservation of liquid water temperature  $T_L$  defined as:

273

274

$$T_L = T - \frac{L_v}{C_p}(q_l + q_r) - \frac{L_s}{C_p}(q_i + q_s).$$

275 Given that  $dT_L = 0$ , the rate of change of the temperature is given by the following  
276 equation:

277

278

$$\frac{\partial T}{\partial t} = \sum_{x=1}^m \frac{L(x)}{C_p} \left( \frac{dq_x}{dt} - D_{q_x} - \frac{1}{\rho} \frac{\partial}{\partial z} (\rho V_x q_x) \right)$$

279

280 where  $L(x)$  is the latent heat of fusion or evaporation, depending on the process  
281 considered,  $Dq_x$  is the convective detrainment and the third term in brackets is the  
282 sedimentation term.

283 At the end of each time step a check is carried out of the conservation of total water and  
284 moist static energy:

$$h = C_p T + gz + Lq_x.$$

285 The scheme is tunable through parameters in the *&microparam* section of the namelist  
286 (RegCM-4.7.1/Doc/README.namelist; Elguindi et al. 2017).

287

288 **WSM5 Scheme**

289 RegCM4-NH also employs the Single-Moment 5-class microphysics scheme of the WRF  
290 model (Skamarock et al., 2008). This scheme (ipptls = 3 in &microparam) follows Hong  
291 et al. (2004) and, similarly to Nogherotto et al. (2016), includes vapor, rain, snow, cloud  
292 ice, and cloud water hydrometeors. The scheme separately treats ice and water  
293 saturation processes, assuming water hydrometeors for temperatures above freezing,  
294 and cloud ice and snow below the freezing level (Dudhia, 1989, Hong et al., 1998). It  
295 accounts for supercooled water and a gradual melting of snow below the melting layer  
296 (Hong et al., 2004, and Hong and Lim, 2006). Therefore, the WSM5 and Nogherotto-  
297 Tompkins schemes have similar structures (Figure 2), but also important differences.

298 Differently from the Nogherotto-Tompkins scheme, the WSM5 (as well as the other WSM  
299 schemes in WRF) prescribes an inverse exponential continuous distribution of particle  
300 size (ex. Marshall and Palmer (1948) for rain, Gunn and Marshall (1958) for snow). It also  
301 includes the size distribution of ice particles and, as a major novelty, the definition of the  
302 number of ice crystals based on ice mass content rather than temperature. Both the  
303 Nogherotto-Tompkins and WSM5 schemes include autoconversion, i.e. sub-time step  
304 processes of conversion of cloud water to rain and cloud ice to snow. For rain, Hong et  
305 al. (2004) use a Kessler (1969) type algorithm in WSM5, but with a stronger physical basis  
306 following Tripoli and Cotton (1980). The Nogherotto-Tompkins scheme also includes the  
307 original Kessler (1969) formula as an option, but it makes available other three  
308 exponential approaches following Sundqvist et al. (1989), Beheng (1994), and  
309 Khairoutdinov and Kogan (2000). For ice autoconversion the Nogherotto-Tompkins  
310 scheme uses an exponential approach (Sundqvist, 1989) with a specific coefficient for ice  
311 particles (following Lin et al., 1983) depending on temperature, while the WSM5 uses a  
312 critical value of ice mixing ratio (depending on air density) and a maximum allowed ice  
313 crystal mass (following Rutledge and Hobbs, 1983) that suppresses the process at low  
314 temperatures because of the effect of air density. Finally, the WSM5 has no dependency  
315 on cloud cover for condensation processes while the Nogherotto-Tompkins scheme uses  
316 cloud cover to regulate the condensation rate in the formation of stratiform clouds.

317 **Illustrative case studies**

318

319 Three case studies (Table 2) of Heavy Precipitation Events (HPE) have been identified in  
320 order to test and illustrate the behavior of the non-hydrostatic core of the RegCM4-NH,  
321 with focus on the explicit simulation of convection over different regions of the world. In  
322 two of the test cases, California and Lake Victoria, data from the ERA-Interim reanalysis  
323 (Dee et al. 2011) are used to provide initial and lateral meteorological boundary conditions  
324 (every 6 hours) for an intermediate resolution run (grid spacing of 12 km, with use of  
325 convection parameterizations), which then provides driving boundary conditions for the  
326 convection-permitting experiments (Figure 3). In the Texas case study, however, we  
327 nested the model directly in the ERA-Interim reanalysis, given that such configuration  
328 was able to accurately reproduce the HPE intensity. In this case the model uses a large  
329 LBC relaxation zone which allows the description of realistic fine-scale features driving  
330 this weather event (although not fully consistent with the Matte et al. (2017) criteria). All  
331 simulations start 24-48 hours before the HPE (Table 2). The analysis focuses on the total  
332 accumulated precipitation over the entire model domain at 3 km resolution (Figure 2) for  
333 the periods defined in Table 2. In the cases of California and Texas the evaluation also  
334 includes the time series of 6 hourly accumulated precipitation averaged on the region of  
335 maximum precipitation (black rectangles in Figures 5a and 7a) because high temporal  
336 resolution observations (NCEP/CPC) are also available (Table 3). The discussion of the  
337 case studies is presented in the next sections; the configuration files (namelists) with full  
338 settings for the three test cases are available at <https://zenodo.org/record/5106399>.  
339

Deleted:

Deleted: (Figure 3)

Deleted: with boundary conditions provided every 6 hours,...

Deleted: accurately

Deleted: even if

Deleted: .

Deleted: .

Deleted: .

Deleted: 4,

Deleted: against available

340 A key issue concerning the use of CP-RCMs is the availability of very high resolution,  
341 high quality observed datasets for the assessment and evaluation of the models, which  
342 is lacking for most of the world regions. Precipitation measurements come from  
343 essentially three distinct sources: in-situ rain-gauges, ground radar and satellite. In the  
344 present study we use 7 observational datasets depending on the case study and the area  
345 covered, as described in Table 3. We have used: Precipitation Estimation from Remotely  
346 Sensed Information using Artificial Neural Networks - Climate Data Record (PERSIAN-  
347 CDR), Climate Hazards Group InfraRed Precipitation with Station data (CHIRPS), the  
348 Climate Prediction Center morphing method (CMORPH), Tropical Rainfall Measuring  
349 Mission (TRMM), NCEP/CPC-Four Kilometer Precipitation Set Gauge and Radar

Deleted: not there

362 (NCEP/CPC), CPC-Unified gauge-based daily precipitation estimates (CPC) and  
 363 Parameter-elevation Regressions on Independent Slopes Model (PRISM) (Table 3).  
 364 NCEP/CPC is a precipitation analysis which merges a rain gauge dataset with radar  
 365 estimates. CMORPH and PERSIAN-CDR are based on satellite measurements, CHIRPS  
 366 incorporates satellite imagery with in-situ station data. CPC is a gauge-based analysis of  
 367 daily precipitation. The PRISM dataset gathers climate observations from a wide range  
 368 of monitoring networks, applying sophisticated quality control measures, and developing  
 369 spatial climate datasets which incorporate a variety of modeling techniques at multiple  
 370 spatial and temporal resolutions.

371

Case	ACRONYM	Region of The event	Domains size x lat x vertical levels	Simulation Window <u>(UTC)</u>	Time
1	CAL	California	480 x 440 x 41	15 Feb 2004 00:00 19 Feb 2004 00:00	
2	TEX	Texas	480 x 440 x 41	9 June 2010 00:00 12 June 2010 00:00	
3	LKV	Lake Victoria	550 x 530 x 41	25 Nov 1999 00:00 1 Dec 1999 00:00	

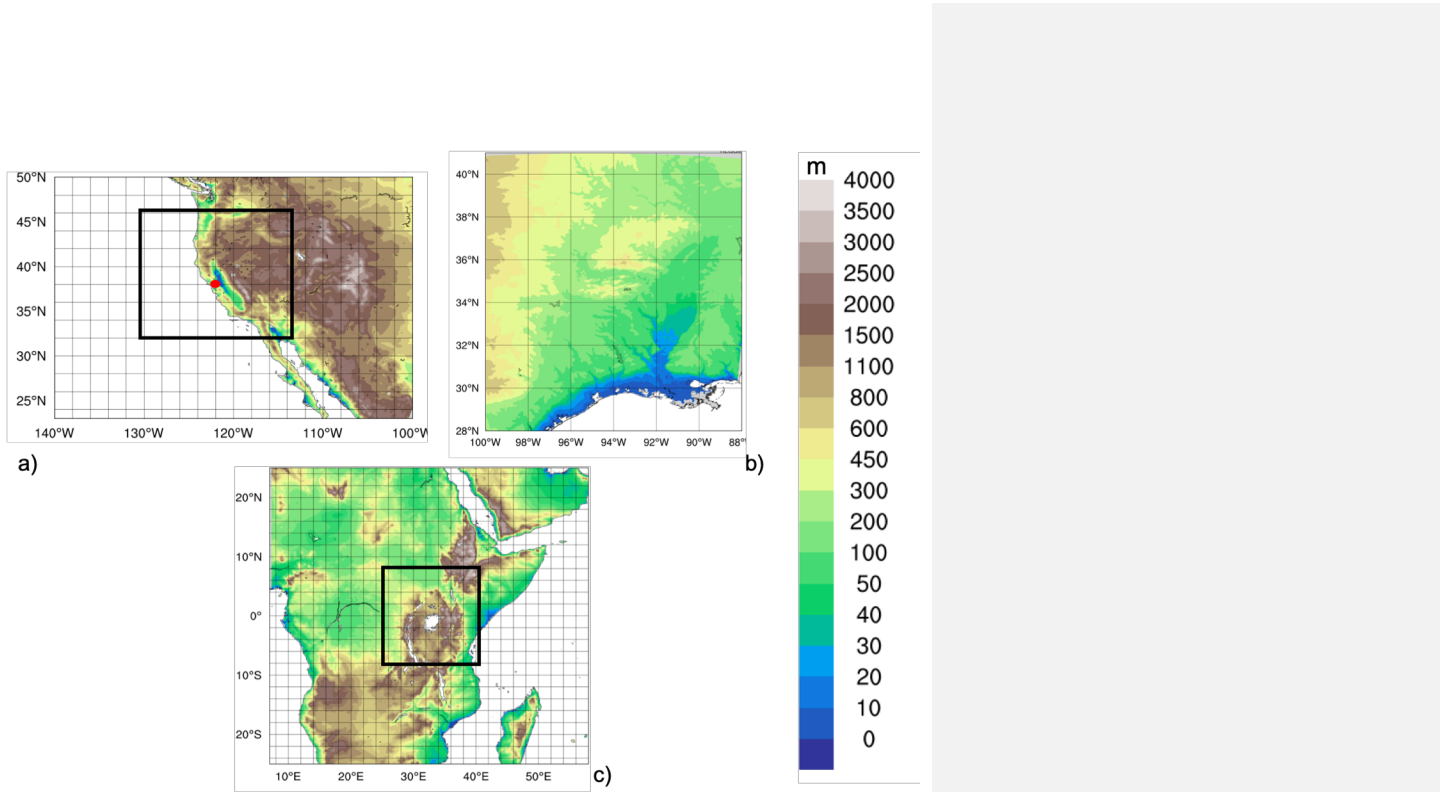
372 **Table 2: List of acronyms and description of the test cases with corresponding**  
 373 **3km domain sizes and simulation period.**

374

Dataset name	Region	Spatial Resolution	Temporal Resolution	Data Source	Reference
TRMM	World	0.5°	Daily	Satellite	Huffman et al. (2007)

CHIRPS	World	0.05°	Daily	Station data+Satellite	Funk et al. (2015)
CMORPH	World	0.25°	Daily	Satellite	Joyce et al. (2004)
NCEP/CPC	USA	0.04°	Hourly	Gauge and Radar	<a href="https://doi.org/10.5065/D69Z93M3">https://doi.org/10.5065/D69Z93M3</a> . Accessed: 27/06/2018
CPC	World	0.5°	Daily	Station data	Chen and Xie (2008)
PRISM	USA	0.04°	Daily	Station data	PRISM Climate Group. 2016.
PERSIAN-CDR	World	0.25°	Daily	Satellite	Ashouri et al. (2015)

383 **Table 3: List of observed precipitation datasets used for comparison.**



385

386 **Figure 3: Domains tested , a) California (CAL) , b) Texas (TEX), c) Lake Victoria**  
 387 (LKV) . For CAL (a) and LKV (b) the black square shows the 3 km simulation  
 388 domains nested in the 12 km domain in figure. For TEX\_case (b) the 3 km domain  
 389 simulation is fed directly with the ERA-Interim reanalysis fields.

Deleted: Simulation d

390

391

## 392 California

393 The first case, referred to as CAL in Table 2, is a HPE which occurred on February 16-18  
 394 2004, producing flooding conditions for the Russian River, a southward-flowing river in  
 395 the Sonoma and Mendocino counties of northern California (red-dot in Figure 3a). The  
 396 event is documented in detail by Ralph et al. (2006), who focused their attention on the  
 397 impact of narrow filament-shaped structures of strong horizontal water vapor transport

Deleted: (California)

Deleted: 1

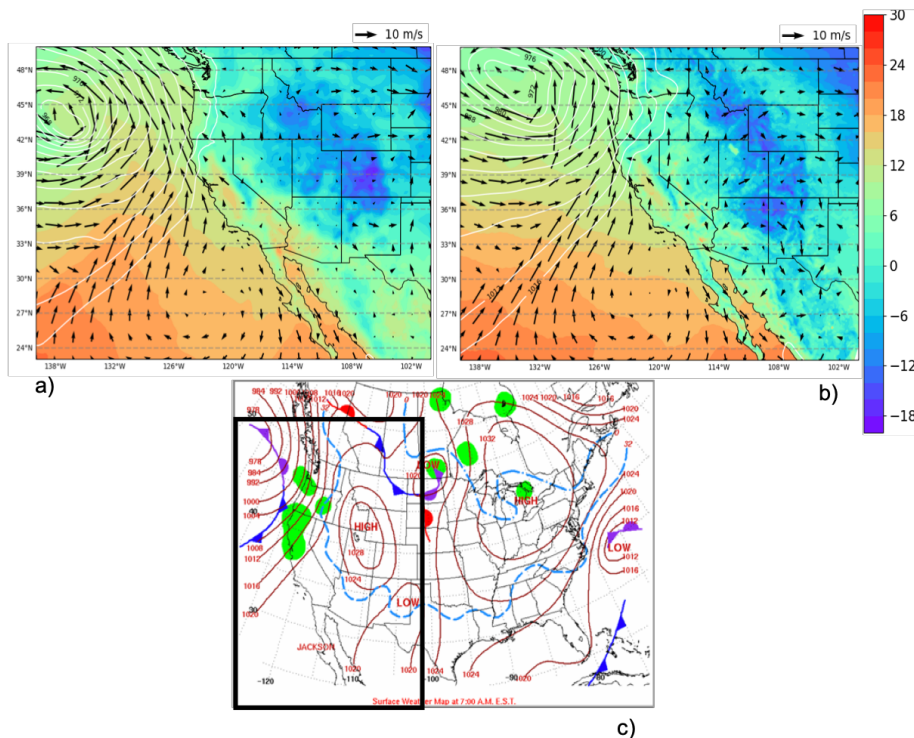
Deleted: 16-18

Deleted: ) (

403 over the eastern Pacific Ocean and the western U.S. coast, called Atmospheric Rivers  
 404 (ARs). ARs are typically associated with a low-level jet stream ahead of the cold front of  
 405 extratropical cyclones (Zhu and Newell 1998; Dacre et al. 2015; Ralph et al. 2018), and  
 406 can induce heavy precipitation where they make landfall and are forced to rise over  
 407 mountain chains (Gimeno et al. 2014). The CAL event consists of a slow propagating  
 408 surface front arching southeastward towards Oregon and then southwestward offshore  
 409 of California (Figure 4a,c). Rain began over the coastal mountains of the Russian River  
 410 watershed at 0700 UTC of February 16, as a warm front descended southward, and also  
 411 coincided with the development of orographically favoured low-level upslope flow (Ralph  
 412 et al. 2006).

Deleted: , 16

Deleted: (



413

414 **Figure 4:** a,b) mean sea level pressure (mslp, hPa, white contour lines), surface  
 415 temperature (color shading, °C) and 100-m wind direction (black arrows, m/s) at 0700 UTC,

Deleted: )(

Deleted: )(

Deleted:

Deleted: )(

Deleted: :

423 February 16, 2004 of ERA5 reanalysis and RegCM 12km respectively. c) NCEP-NOA  
424 **Surface Analysis of pressure and fronts. The black box in (c) bounded the area represented**  
425 **in (a) and (b)**

Deleted: 16

Deleted: .

426 The intermediate resolution (12 km) domain (Figure 3a) covers a wide area  
427 encompassing California and a large portion of the coastal Pacific Ocean, with 23 vertical  
428 levels and a parameterization for deep convection based on the Kain–Fritsch scheme  
429 (Kain, 2004). The ERA-Interim driven simulation is initialized at 0000 UTC, February 15  
430 2004 (Table 2) and lasts until 0000 UTC February 19 2004. This simulation is used as a  
431 boundary conditions for a RegCM4-NH run over a smaller area centered over northern  
432 California (Fig. 3a) at 3 km horizontal resolution, with 41 vertical levels and boundary  
433 conditions updated every 6 hours. In RegCM4-NH only the shallow convection code of  
434 the Tiedtke scheme (Tiedtke, 1996) is activated. Simulated precipitation is compared  
435 with the CHIRPS, CMORPH, TRMM, PRISM, NCEP/CPC observations (Table 3).

Deleted: 15

Deleted: 19

Deleted: drives a corresponding

Deleted: using a

Deleted: domain

Deleted: 2

Deleted: grid spacing

Deleted: and

Deleted: , with

Deleted: at

Deleted: intervals

Deleted: component

Deleted: described in

Deleted: .

Deleted: First, we notice

Deleted: that

Deleted: on 14 Feb at 7:00 am characteristic

Deleted: which are fed into the RegCM4-NH model,

Deleted: 3

Deleted: , as shown in Figure 4, where we compare the mean sea level pressure (mslp), surface temperature and wind direction on 14 Feb at 7:00 am, as simulated by RegCM at 12 km (Fig.43b) with corresponding fields from the ERA5 reanalysis (Fig.4a).

Deleted: places

436 As shown in Figure 4, the February 16 synoptic conditions for mean sea level pressure  
437 (mslp), surface temperature and wind direction, of this case study, are well reproduced by  
438 RegCM4 at 12 km (Fig. 4b) when compared to ERA5 reanalysis (Fig. 4a). The surface  
439 analysis of pressure and fronts derived from the operational weather maps prepared at  
440 the National Centers for Environmental Prediction, Hydrometeorological Prediction  
441 Center, National Weather Service  
442 ([https://www.wpc.ncep.noaa.gov/dailywxmap/index\\_20040216.html](https://www.wpc.ncep.noaa.gov/dailywxmap/index_20040216.html)) is also reported in  
443 Figure 4c.

444 The available observed precipitation datasets show similar patterns for the total  
445 accumulated precipitation (Figure 5), in particular CHIRPS (Figure 5a), PRISM (Figure  
446 5d) and NCEP (Figure 5e) exhibit similar spatial details and magnitudes of extremes.  
447 CHIRPS shows, a maximum around 42°N which is not found in the other datasets.  
448 CMORPH (Figure 5b) and TRMM (Figure 5c) show lower precipitation maxima and lesser  
449 spatial details due to their lower resolution, indicating that the performance of satellite-  
450 based products may be insufficient as a stand alone product to validate the model for this  
451 case.

479 The largest observed maxima are placed on the terrain peaks, with extreme rainfall  
480 greater than 250 mm in 60 hours over the coastal mountains and between 100 – 175 mm  
481 elsewhere (Fig. 5). The black box in Fig 5a shows the area of the Russian River  
482 watershed where the largest rainfall rates were detected (269 mm and 124 mm in 60-h  
483 accumulated rainfall between 0000 UTC February 16 and 1200 UTC February 18, 2004,  
484 respectively). (Ralph et al., 2006).

485 The convection-permitting simulation captures the basic features of the observed  
486 precipitation, both in terms of spatial distribution (Fig. 5f) and of temporal evolution of  
487 rainfall (Fig. 6a). However, it shows higher precipitation rates than observed over the sea  
488 and over the mountain chains, with lower intensities than observed in the south-east part  
489 of the mountain chain (Fig. 5). The 12-km simulation instead severely underestimates the  
490 magnitude of the event (Fig. 5g).

491 Figure 6a shows the 6-hourly accumulated precipitation averaged over the black box in  
492 Figure 5a. The 3 km and 12 km simulations capture the onset of the event, but the peak  
493 intensity is strongly underestimated by the 12 km run, while it is well simulated by the 3  
494 km run, although the secondary maximum is overestimated. These results demonstrate  
495 that only the high resolution convection-permitting model is able to captures this extreme  
496 event, and that parameterized convection has severe limits in this regard (Done et al.  
497 2004; Lean et al. 2008; Weisman et al. 2008; Weusthoff et al. 2010; Schwartz 2014; Clark  
498 et al. 2016).

Deleted: In general, the observed precipitation datasets place Tt...

Deleted: highest

Deleted: greater

Deleted: than

Deleted: a

Deleted: ,

Deleted: highlighting the locations of the observing systems, including Cazadero (CZD) and Bodega Bay (BBY) where the largest rainfall rates were detected, 269 mm and 124 mm in 60-h accumulated rainfall between 0000 UTC 16 February and 1200 UTC 18 February 2004, respectively

Deleted: , as shown for example in Fig. 5

Deleted: By contrast, t

Deleted: instead, severely

Deleted: precipitation

Deleted: Concerning the timing and intensity of the event in the CZD subregion,

Deleted:

Deleted: (Fig.6a)

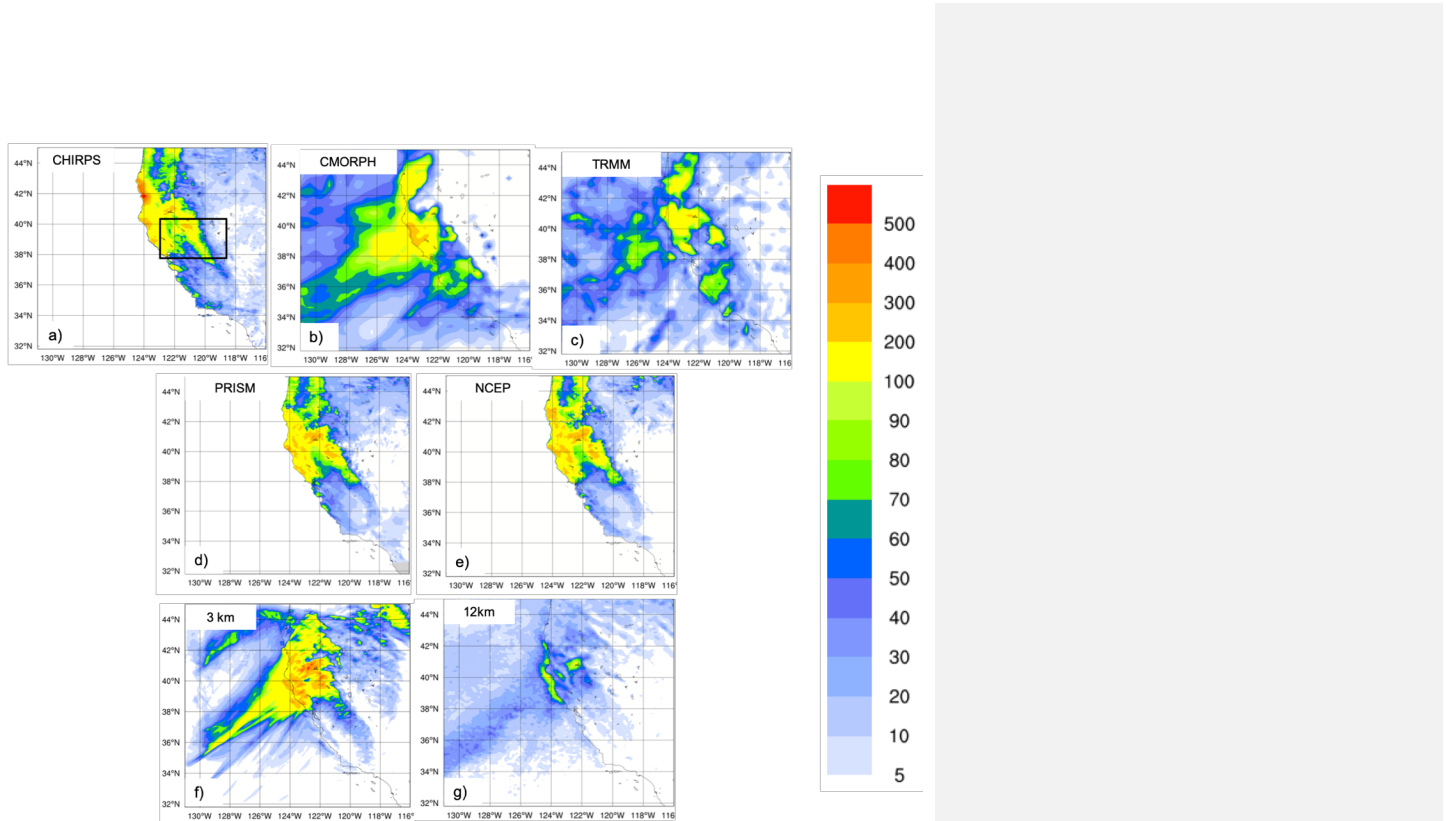
Deleted: of

Deleted: ,

Deleted: shows that Both both

Deleted: the

Deleted: before, our



525

526 **Figure 5 : Total accumulated precipitation (mm) during the California case: CHIRPS (a),**  
 527 **CMORPH (b), TRMM (c) observations, PRISM (d) and NCEP Reanalysis (e) and convection-**  
 528 **permitting simulation with RegCM4-NH at 3km (f) and RegCM4 at 12km (g). The black box**  
 529 **denotes the area where the spatial average of 6-hourly accumulated precipitation is**  
 530 **calculated for Figure 6a.**

Deleted: (top line)

Deleted: (middle line)

Deleted: bottom line

Deleted:

531

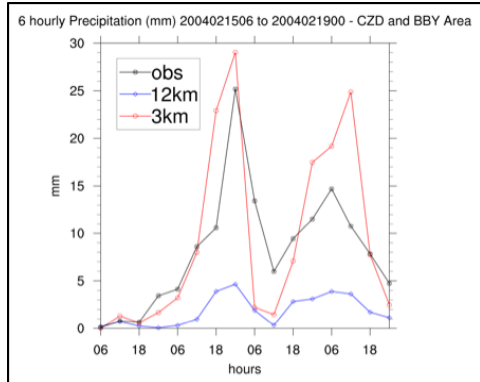
532

533

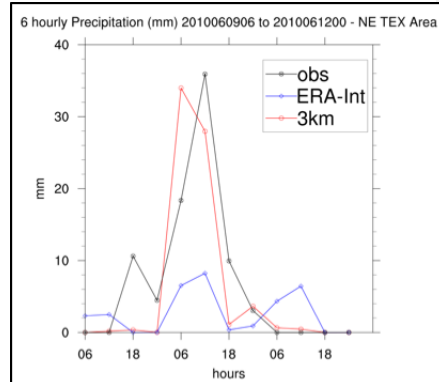
534

535

CAL (a)



TEX (b)



540 **Figure 6: Time series of the 6 hourly accumulated precipitation (in mm on the y-axis) during**  
 541 **the CAL event (a) and during the TEX event (b). The blue lines show RegCM4 12 Km and**  
 542 **ERA interim 6 hourly accumulated precipitation averaged over the areas indicated by the**  
 543 **black squares in Figures 5 and 7, while the red line shows the 6 hourly accumulated**  
 544 **precipitation simulated by RegCM4-NH. The observations are shown with a black line.**

545

546 **Texas**

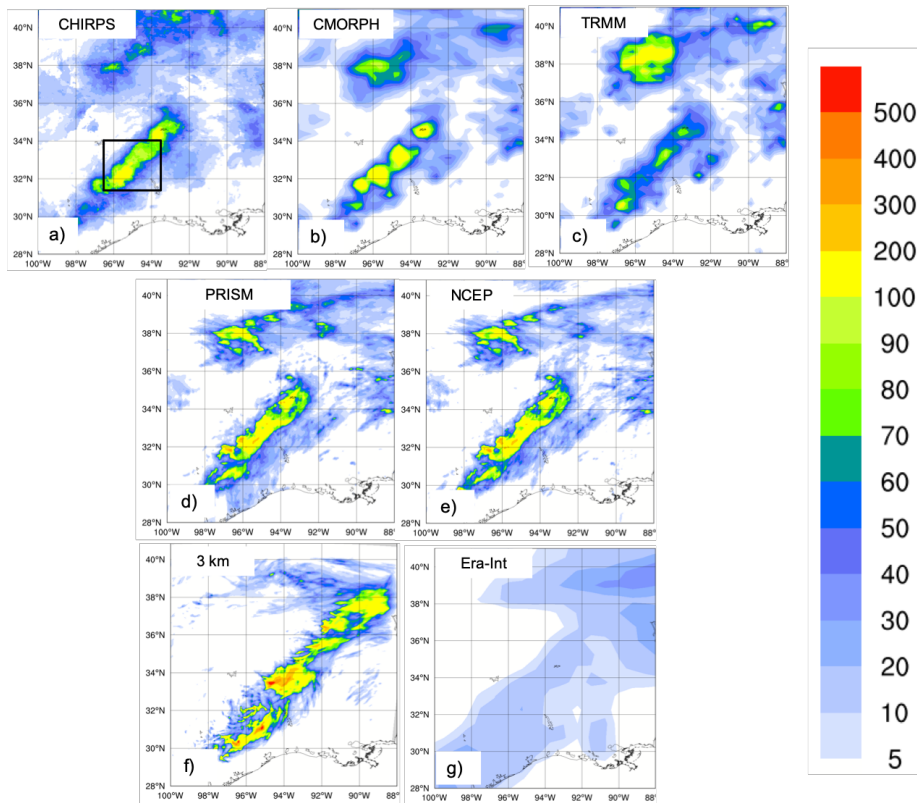
547 Case 2, hereafter referred to as TEX (Table 2), is a convective precipitation episode  
 548 exhibiting characteristics of the “Maya Express” flood events, linking tropical moisture  
 549 plumes from the Caribbean and Gulf of Mexico to midlatitude flooding over the central  
 550 United States (Higgins 2011). During the TEX event, an upper-level cutoff low over  
 551 northeastern Texas, embedded within a synoptic-scale ridge, moved slowly  
 552 northeasterward. Strong low-level flow and moisture transport from the western Gulf of  
 553 Mexico progressed northward across eastern Texas. The event was characterized by  
 554 low-level moisture convergence, weak upper-level flow, weak vertical wind shear, and  
 555 relatively cold air (center of cutoff low), which favored the slow-moving convective storms  
 556 and nearly stationary thunderstorm outflow boundaries. The main flooding event in

Deleted: red  
 Deleted: 3  
 Deleted: (a,b)

Deleted: 1

561 eastern Texas occurred on June 10, 2010, with a daily maximum rainfall of 216.4 mm ~~for~~  
562 the region in the black box of Figure 7a (Higgins 2011).

Deleted: of



564 Figure 7: Total accumulated precipitation (mm) during the Texas case: CHIRPS (a),  
565 CMORPH (b), TRMM (c), PRISM (d), NCEP Reanalysis (e) and convection-permitting  
566 simulation with RegCM4-NH at 3 km grid spacing (f) and ERA-Interim (g). The black box (a)  
567 shows the area where the spatial average of 6-hourly accumulated precipitation was  
568 calculated for Figure 6b

Deleted: observations (top line)

Deleted: and

Deleted: (central line)

Deleted: Era-Int

Deleted: bottom line

569 As for the California case, the observed precipitation datasets show coherent patterns for  
570 the total accumulated precipitation (Figure 7), with the highest values related to the  
571 mesoscale convective system in eastern Texas (~ 200 mm), and another smaller area of

Deleted: 6

579 high precipitation more to the north, approximately over Oklahoma. PRISM (Figure  
580 7d) and NCEP (Figure 7e) capture similar spatial details and magnitudes of extremes,  
581 CHIRPS (Figure 7a) has lower precipitation extremes in the north compared to the other  
582 datasets, while CMORPH (Figure 7b) and TRMM (Figure 7c) show the lowest  
583 precipitation extremes and reduced spatial details as already noted for the California  
584 case.

585 Figure 7f and Figure 7g present precipitation as produced by the RegCM4-NH and the  
586 ERA-Interim reanalysis (driving data), respectively. ERA-Interim reproduces some of the  
587 observed features of precipitation, but with a substantial underestimation over the areas  
588 of maximum precipitation because of its coarse resolution. By comparison, the RegCM4-  
589 NH simulation (Fig. 7f) shows an improvement in both pattern and intensity of  
590 precipitation, and is substantially closer to observations over eastern Texas. However,  
591 the precipitation area is slightly overestimated and the model is not capable of  
592 reproducing the small region of maximum precipitation in the north.

593  
594 The time series of precipitation over eastern Texas from June 9 to 12, 2010 for  
595 observations (black line), ERA-Interim (blue line) and RegCM4-NH (red line) are reported  
596 in figure 6b. Precipitation increases over this region from 0000 UTC until it reaches the  
597 observed maximum at 1200 UTC, on June 10 (~35 mm), gradually decreasing afterwards  
598 until 0600 UTC, on June 11. The RegCM4-NH simulation shows a more realistic temporal  
599 evolution than the ERA-Interim, which exhibits an overall underestimation of precipitation.  
600 The non-hydrostatic model produces precipitation values closer to the observations,  
601 however, the simulated maximum is reached 6 hours earlier than observed.

602

603

#### 604 Lake Victoria

605 Case 3 focuses on Lake Victoria (LKV), with the purpose of testing RegCM4-NH on a  
606 complex and challenging region in terms of convective rainfall. It is estimated that each  
607 year 3,000-5,000 fishermen perish on the lake due to nightly storms (Red Cross, 2014).  
608 In the Lake Victoria basin, the diurnal cycle of convection is strongly influenced by  
609 lake/land breezes driven by the thermal gradient between the lake surface and the

Deleted:

Deleted:

Deleted: The bottom panels in

Deleted: I

Deleted:

Deleted:

Deleted: ,

Deleted: 6

Deleted: June

Deleted: :

Deleted: , 10 June,

Deleted: :

Deleted: June

Deleted: :

Deleted: June

Deleted: In general, t

Deleted: ,

627 surrounding land. As the land warms during the course of the day, a lake breeze is  
628 generated which flows from the relatively cooler water towards the warmer land surface.  
629 The circulation is effectively reversed at night, when the land surface becomes cooler  
630 than the lake surface, leading to convergence over the lake and associated thermal  
631 instability.

632 In the LKV region, prevailing winds are generally easterly most of the year with some  
633 variability due to the movement of the ITCZ. The local diurnal circulation created by the  
634 presence of the lake creates two diurnal rainfall maxima. During daylight hours, when the  
635 lake breeze begins to advance inland, convergence is maximized on the eastern coast of  
636 the lake as the lake breeze interacts with the prevailing easterlies. Studies have also  
637 noted the importance of downslope katabatic winds along the mountains to the east of  
638 the lake in facilitating convergence along the eastern coastal regions (Anyah et al. 2006).  
639 This creates a maximum in rainfall and convection on the eastern coast of LKV.  
640 Conversely, during nighttime hours, when the local lake circulation switches to flow from  
641 the land towards the lake, the prevailing easterlies create locally strong easterly flow  
642 across the lake and an associated maximum in convergence and rainfall on the western  
643 side of LKV.

644 The LKV simulation starts on November 25, 1999 and extends to the beginning of  
645 December 1999 (Table 2), covering a 5-day period which falls within the short-rain season  
646 of East Africa. The choice of 1999, an ENSO neutral year, was made in order to focus the  
647 analysis on local effects, such as the diurnal convection cycle in response to the lake/land  
648 breeze, with no influence of anomalous large scale conditions. A 1-dimensional lake  
649 model (Hostetler et al. 1993; Bennington et al. 2014) interactively coupled to RegCM4-  
650 NH was utilized to calculate the lake surface temperature (LST), since lake-atmosphere  
651 coupling has been shown to be important for LKV (Sun et al. 2015; Song et al. 2004).  
652 This coupled lake model has been already used for other lakes, including Lake Malawi in  
653 southern Africa (Diallo et al. 2018). As with the other experiments, the boundary  
654 conditions are provided by a corresponding 12 km RegCM4 simulation employing the  
655 convection scheme of Tiedtke (1996).

Deleted: within the larger scale easterly wind field

Deleted: 25

Deleted: the

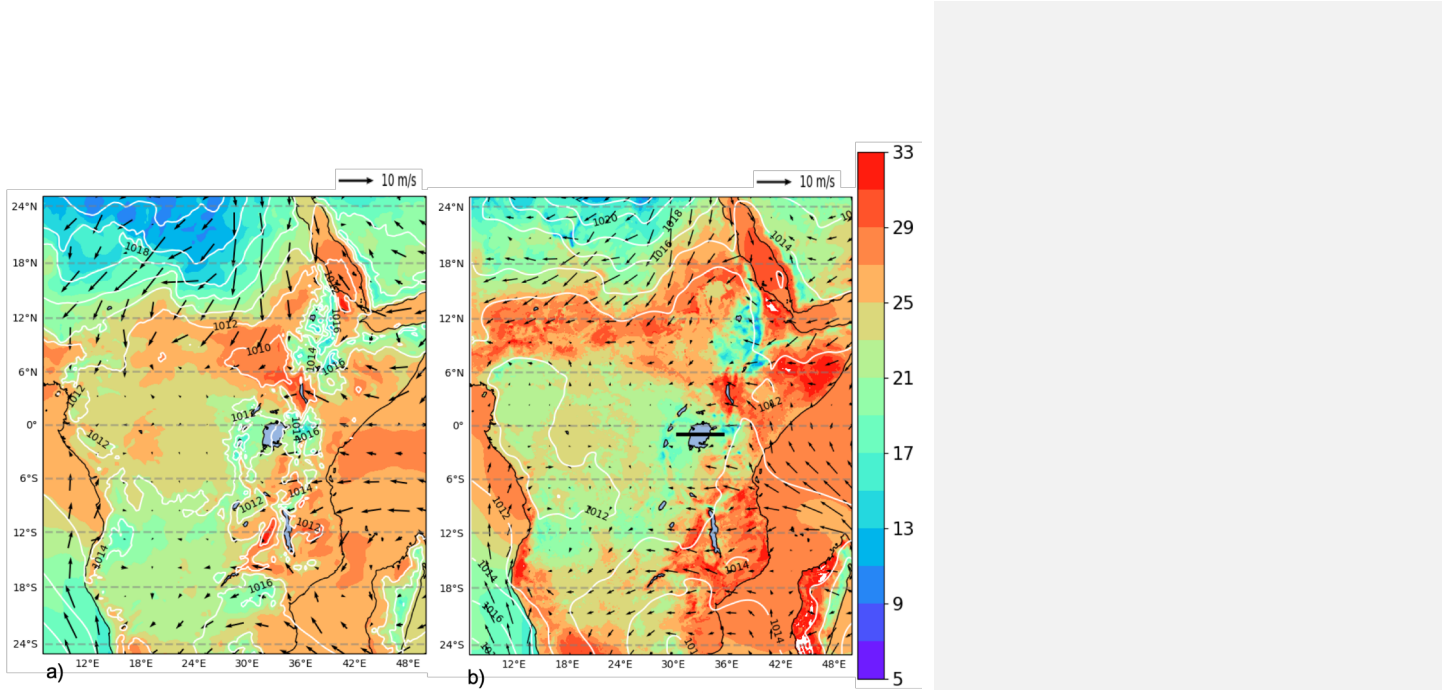
659 At the beginning of the simulation, the LST over the lake is uniformly set to 26°C, and is  
660 then allowed to evolve according to the lake-atmosphere coupling. This initial LST value  
661 is based on previous studies. For example, Talling (1969) finds Lake Victoria surface  
662 temperatures ranging from 24.5-26°C during the course of the year. Several studies have  
663 used RCMs to investigate the Lake Victoria climate (Anyah et al., 2006; Anyah and  
664 Semazzi 2009, Sun et al. 2015), and found a significant relationship between lake  
665 temperature and rainfall depending on season. The value of 26°C is typical of the winter  
666 season and was chosen based on preliminary sensitivity tests using different values of  
667 initial temperature ranging from 24°C to 26°C.

668 The synoptic feature favorable for the production of precipitation over the LKV in this  
669 period corresponds to a large area of southeasterly flow from the Indian Ocean (Fig. 8a),  
670 which brings low-level warm moist air into the LKV region ~~facilitating the production of~~  
671 convective instability and precipitation. This synoptic situation, with a low-level south-  
672 easterly jet off the Indian Ocean, is a common feature associated with high precipitation  
673 in the area (Anyah et al. 2006), ~~and can be seen~~ in ERA5 ~~data~~ (Figure 8a). ~~Although~~  
674 ~~some bias in terms of magnitude, this is reasonably well reproduce by the 12 km~~  
675 ~~simulation (Figure 8b).~~

Deleted:

Deleted: is found

Deleted: 7



679

680 **Figure 8: Mean sea level pressure (mslp) (hPa) (white contour lines), surface temperature**  
 681 **(color shading) (°C) and 100-m wind (black arrows) averaged over the period 25 November**  
 682 **0000 UTC - 1 December 0000 UTC, by ERA5 reanalysis (a) and RegCM 12km (b). The black**  
 683 **line (b) shows the cross-section position represented in Fig. 9**

684 The LKV region dynamics are quite distinct between nighttime and daytime and the  
 685 rainfall in and around the lake has a pronounced diurnal cycle. To understand this strong  
 686 diurnal cycle, Figure 9 shows a cross-section through the lake (32E to 34E, black line in  
 687 right panel of Fig. 8b) along 1°S latitude at a period during strong nighttime (Fig. 9b,d;  
 688 0600Z November 30) and daytime convection (Figure 9a,c; 12Z November 29). Wind  
 689 vectors in Figure 9 show the zonal-wind anomaly across 0°-2°S to highlight the  
 690 circulations associated with LKV. During the day, surface heating around the lake leads  
 691 to a temperature difference between the land and lake sufficient to generate a lake  
 692 breeze, which causes divergence over the lake, while over the highlands to the east the  
 693 environment is more conducive to convection where convergence is focused (9a,c).  
 694 Conversely, during the night, a land breeze circulation is generated, which induces  
 695 convergence and convection over the lake (Figure 9b,d). In Figure 10, the evolution of

Deleted: black  
 Deleted: direction  
 Deleted:  
 Deleted:  
 Deleted:  
 Deleted: of  
 Deleted: .

Deleted: 7  
 Deleted: 30  
 Deleted: .  
 Deleted: 29

Deleted: tial  
 Deleted: surrounding  
 Deleted:  
 Deleted: .

711 the nighttime land breeze is illustrated with cooler temperature anomalies propagating  
712 westward onto the lake during the night.

713 Comparing the 3 km simulation to the 12 km forcing run, we find that the localized  
714 circulations created by local forcings (i.e. convection) are much stronger in the convection  
715 permitting resolution experiment. We also find stronger and more localized areas of  
716 convective updrafts compared to the 12 km simulation (Figure 9c,d; omega is shown  
717 instead of vertical velocity here because of the difference in dynamical core). As an  
718 example during the nighttime event (Figure 9b,d), there is a broad area of upward motion  
719 over the lake and the associated broad convergence in the 12km simulation, while in the  
720 convection permitting 3km simulation, convection is much more local and concentrated  
721 over the western part of the lake. Indeed, nighttime rainfall tends to be concentrated over  
722 the western part of the lake ( Sun et al. 2015; Figure 11a-d). Stronger convection  
723 simulated in the 3 km experiment could also be tied to stronger temperature anomalies  
724 shown over the lake and land and between day and night relative to the 12km simulation  
725 (Figure 10). The 3km simulation also shows a more pronounced land breeze propagation  
726 at night compared to the 12km simulation.

727 This demonstrates that the 3km simulation is better equipped to simulate the localized  
728 circulations associated with this complex land-lake system.

Deleted: high resolution

Deleted: as seen in the vertical velocities (9a,b)

Deleted: 8

Deleted: model output

Deleted: For example Forfor

Deleted: .

Deleted: note the

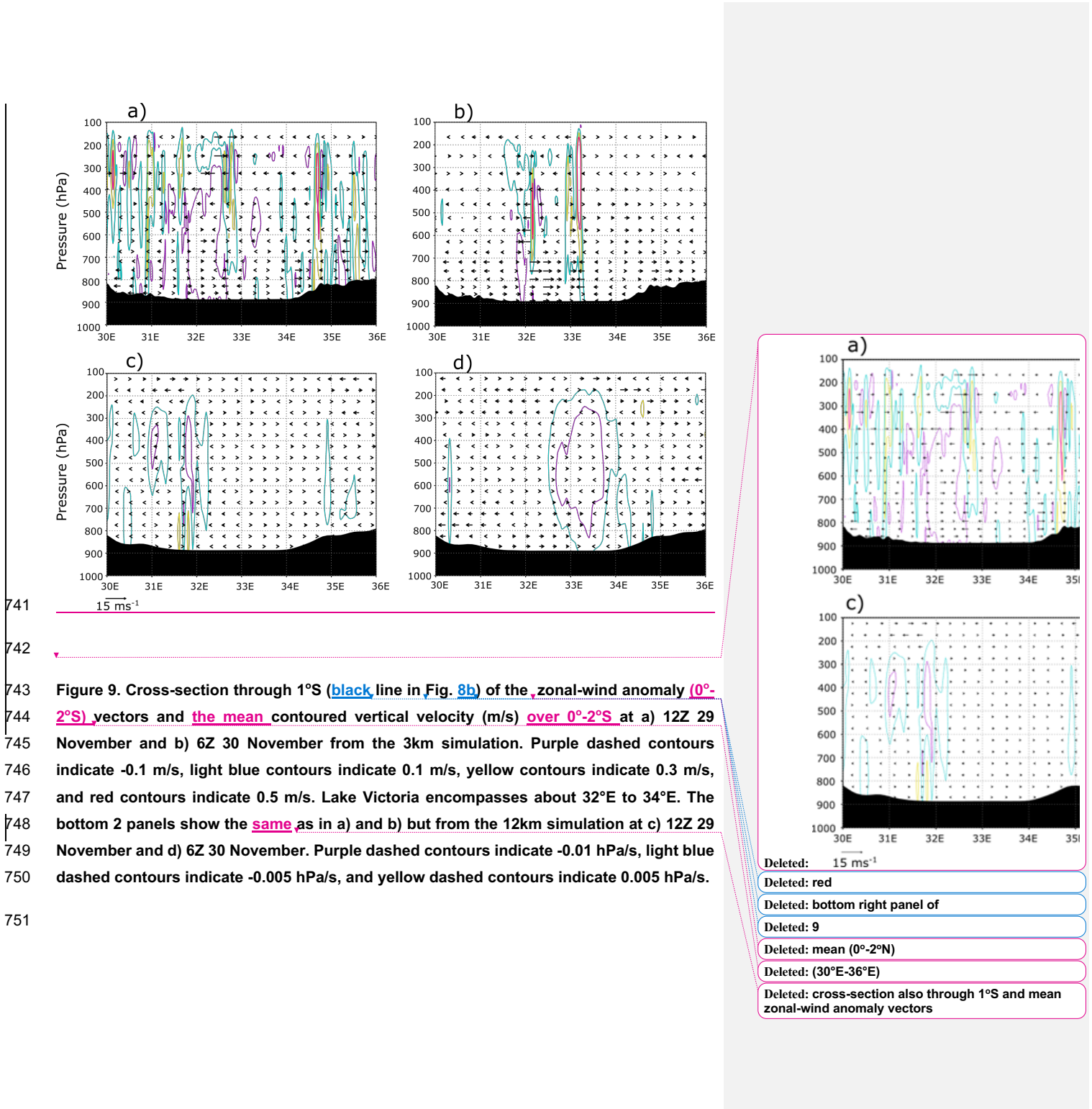
Deleted: .

Deleted: The s

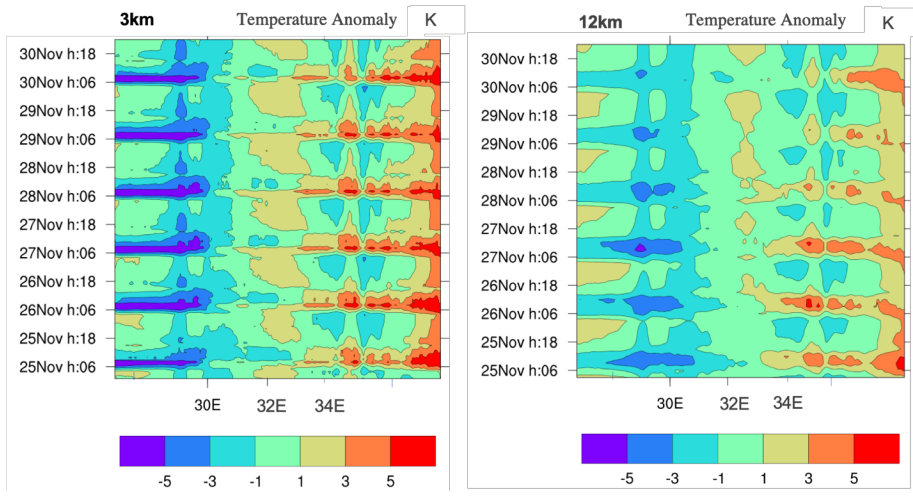
Deleted: is

Deleted: the

Deleted: gradients between



760

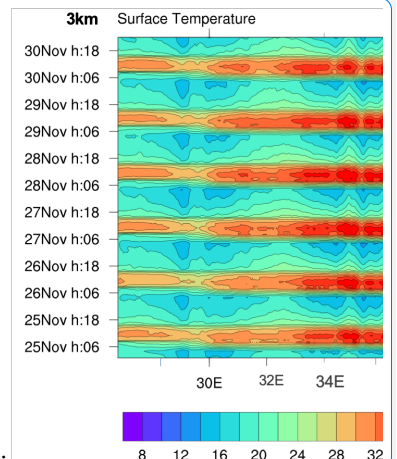


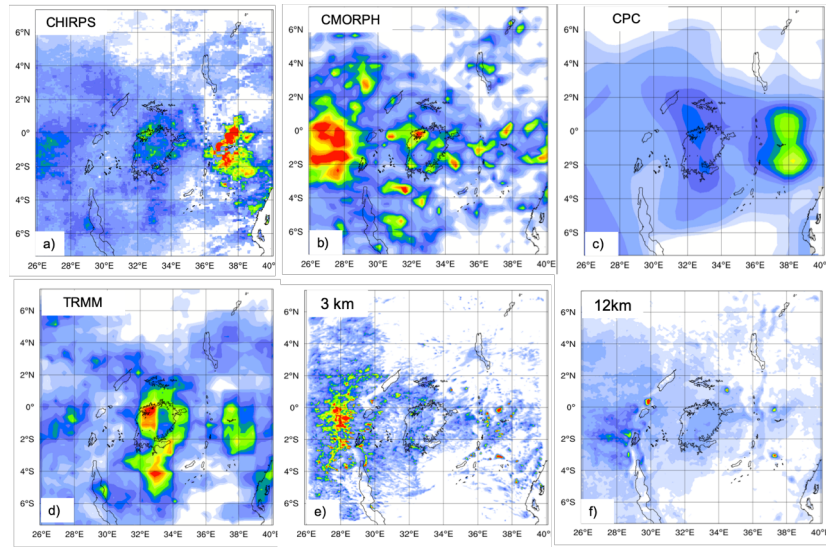
761 **Figure 10 : Longitude-time (hourly) Hovmöller diagram of LKV domain surface temperature  
762 anomaly (shading, in K). Panels correspond to the 3km simulation (left) and 12km  
763 simulation (right). The lake Victoria is between 32°E and 34°E longitude**

764

Deleted: C

Deleted:





767

768 **Figure 11:** Total event accumulated precipitation (mm) during the LKV case (November 25,  
 769 1999-December 1, 1999) measured by CHIRPS (a), CMORPH (b), CPC (d), TRMM (e) and  
 770 calculated by RegCM4 at 3 km (e) and 12 km (f).

771

772 Figure 11 reports the total accumulated precipitation observed and simulated for the LKV  
 773 case. TRMM (Figure 11d) and CPC (Figure 11c) show a similar pattern, with two-rainfall  
 774 maxima of different intensities over the southeastern and northwestern lake areas.  
 775 CMORPH (Figure 11b) shows a western rainfall maximum similar to TRMM and one large  
 776 rainfall area almost entirely centered over the highlands to the west of the lake.  
 777 Conversely in CHIRPS (Figure 11a) a maximum is found to the east of the lake while  
 778 several localized maxima occur over the lake. The differences among the observed  
 779 datasets highlight the issue of observational uncertainty and the need to take into  
 780 consideration shortcomings associated with the types of observational datasets  
 781 considered. Different datasets can have significantly different climatologies, especially in  
 782 areas of low data availability. For example, Prein and Gobiet (2017) analyzed two gauge-  
 783 based European-wide datasets, and seven global low-resolution datasets, and found

Deleted:

Deleted: top left

Deleted: top center

Deleted: (top right)

Deleted: bottom left

Deleted: bottom center

Deleted: bottom right

Deleted:

Deleted: finally

Deleted:

Deleted:

Deleted: between

Deleted: y

Deleted:

798 large differences across the observation products, often of similar magnitude as the  
799 difference among model simulations. In this case and for this area the observation  
800 uncertainty plays a big role especially at high resolution, and highlights the need for an  
801 adequate observational network for model validation. However, despite the large  
802 uncertainty among the different observed datasets (Figure 11 a-d), we find a significant  
803 underestimation of the precipitation by the 12 km run over the lake independently of the  
804 dataset used as a reference (Figure 11f). In contrast, the 3 km simulation (Figure 11e)  
805 shows substantially greater detail, with rainfall patterns more in agreement with the  
806 CMORPH data. In particular, the 3 km simulation reproduces well the local rainfall  
807 maxima on the western side of the lake, although these appear more localized and with  
808 a multi-cell structure compared to CMORPH and TRMM. Additionally, the 12 km  
809 simulation underestimates the observed heavy rainfall totals in the highlands to the west  
810 of the lake region especially when compared to CMORPH, which are instead reproduced  
811 by the 3 km simulation.

Deleted: between

Deleted: .

Deleted:

Deleted: ¶

Deleted: However, even taking into account the elevated uncertainty existing in the observations datasets, we find a significant underestimation of rain amounts in the 12 km run ¶

Deleted: compared to any of them

Deleted:

Deleted:

Deleted: 0

Deleted: , with a wide area of rainfall around 80mm over the whole of LKV...

Deleted:

Deleted: .

Deleted:

Deleted:

812 This last test case demonstrates the ability of RegCM4-NH in simulating realistic  
813 convective activity over a such morphologically complex region, which is a significant  
814 improvement compared to the hydrostatic-coarse resolution model configuration.

815

## 816 **Conclusions and future outlook**

817

818 In this paper we have described the development of RegCM4-NH, a non hydrostatic  
819 version of the regional model system RegCM4, which was completed in response to the  
820 need of moving to simulations at convection-permitting resolutions of a few kilometers.  
821 The non-hydrostatic dynamical core of MM5 has been incorporated into the RegCM4  
822 system previously based on the MM5 hydrostatic core. Some modifications to the MM5  
823 dynamical core were also implemented to increase the model stability for long term runs.  
824 RegCM4-NH also includes two explicit cloud microphysics schemes needed to explicitly  
825 describe convection and cloud processes in the absence of the use of cumulus  
826 convection schemes. Finally, we presented a few case studies of explosive convection to

Deleted: m

Deleted: the non-hydrostatic version of

Deleted: thus

Deleted: ,

Deleted: an approach facilitated by the fact that the this last is essentially an evolution of the MM5

Deleted: .

852 illustrate how the model provides realistic results in different settings and general  
853 improvements compared to the coarser resolution hydrostatic version of RegCM4 for  
854 such types of events.

855

856 As already mentioned, RegCM4-NH is currently being used for different projects, and  
857 within these contexts, is being run at grid spacings of a few kilometers for continuous  
858 decadal simulations, driven by reanalyses of observations or GCM boundary conditions  
859 (with the use of an intermediate resolution domains) over different regions, such as the  
860 Alps, the Eastern Mediterranean, Central-Eastern Europe and the Caribbeans. These  
861 projects, involving multi-model inter-comparisons, indicate that the performance of  
862 RegCM4-NH is generally in line with that of other convection-permitting models, and  
863 exhibits similar improvements compared to coarser resolution models, such as a better  
864 simulation of the precipitation diurnal cycle and of extremes at hourly to daily time scales.  
865 The results obtained within the multi-model context confirm previous results from single-  
866 model studies (Kendon et al. 2012, 2017, Ban et al. 2014, 2015; Prein et al. 2015, 2017),  
867 but also strengthen the robustness of the findings through reduced uncertainty compared  
868 to coarse resolution counterpart (Ban et al., 2021, Pichelli et al., 2021). The convection-  
869 permitting scale can thus open the perspective of more robust projections of future  
870 changes of precipitation, especially over sub-daily time scales.

871

872 One of the problems of the RegCM4-NH dynamical core is that, especially for long runs  
873 with varied meteorological conditions, a relatively short time step is needed, for stability  
874 reasons. This makes the model rather computationally demanding, although not more  
875 than other convection-permitting modeling systems such as the Weather Research and  
876 Forecast model (WRF, Skamarok et al. 2008). For this reason, we are currently  
877 incorporating within the RegCM system a very different and more computationally efficient  
878 non-hydrostatic dynamical core, which will provide the basis for the next version of the  
879 model, RegCM5, to be released in the future.

880

881 Following the philosophy of the RegCM modeling system, RegCM4-NH is intended to be  
882 a public, free, open source community resource for external model users. The non-

Deleted: km

Deleted:

Deleted:

Deleted:

Deleted: short

Deleted: s

Deleted: to be used

890 hydrostatic dynamical core has been implemented in a way that it can be activated in  
891 place of the hydrostatic dynamics through a user-set switch, which makes the use of  
892 RegCM4-NH particularly simple and flexible. We therefore envision that the model will be  
893 increasingly used by a broad community so that a better understanding can be achieved  
894 of its behavior, advantages and limitations.

895

896 **Code availability:** <https://zenodo.org/record/4603556>

897 **Cases study configuration files:** <https://zenodo.org/record/5106399>

898

899

900 **Author contribution:** CE prepared the manuscript with contributions from all co-authors  
901 and coordinated research, SP, TA, GR carried out and analysed the simulations, PE  
902 investigated solutions to stabilize/adapt the model at the km-scale and performed  
903 preliminary validation tests, GG developed/adapted the model code, FDS contributed to  
904 develop the coupled version of the model, NR developed one of the microphysics  
905 scheme, GF supervised and coordinated all activities.

906

907 **Competing interests:** The authors declare that they have no conflict of interest.

908

909

910 References

911 Anyah, R., Semazzi, F. H. M., Xie, L., 2006: Simulated Physical Mechanisms Associated  
912 with Climate Variability over Lake Victoria Basin in East Africa, *Mon. Wea. Rev.*, 134  
913 3588-3609.

914

915 Anthes, R. A., Hsie, E. -Y., & Kuo, Y. -H. (1987). Description of the Penn State/NCAR  
916 Mesoscale Model: Version 4 (MM4) (No. NCAR/TN-282+STR). doi:10.5065/D64B2Z90

917

918 Anyah RO, Semazzi F (2009) Idealized simulation of hydrodynamic characteristics of  
919 Lake Victoria that potentially modulate regional climate. *Int J Climatol* 29(7):971–981.  
920 doi:[10.1002/joc.1795](https://doi.org/10.1002/joc.1795)

921

922 Ashouri, Hamed, Kuo Lin Hsu, Soroosh Sorooshian, Dan K. Braithwaite, Kenneth R.  
923 Knapp, L. Dewayne Cecil, Brian R. Nelson and Olivier P. Prat (2015). 'PERSIANN- CDR:  
924 Daily precipitation climate data record from multisatellite observations for hydrological and  
925 climate studies'. In: *Bulletin of the American Meteorological Society*. ISSN: 00030007.  
926 DOI: 10.1175/BAMS-D-13-00068.1.

927

928 Ban, N., J. Schmidli, and C. Schär, 2014: Evaluation of the convection-resolving regional  
929 climate modeling approach in decade-long simulations. *J. Geophys. Res. Atmos.*, 119,  
930 7889– 7907, <https://doi.org/10.1002/2014JD021478>.

931

932 Ban N, Schmidli J, Schär C (2015) Heavy precipitation in a changing climate: does short-  
933 term summer precipitation increase faster? *Geophys Res Lett* 42:1165–1172.  
934 <https://doi.org/10.1002/2014GL062588>

935 Ban, N., Caillaud, C., Coppola, E. et al. The first multi-model ensemble of regional climate  
936 simulations at kilometer-scale resolution, part I: evaluation of precipitation. *Clim Dyn*  
937 (2021). <https://doi.org/10.1007/s00382-021-05708-w>

938

939 Beheng, K.: A parameterization of warm cloud microphysical conversion processes,  
940 *Atmos. Res.*, 33, 193–206, 1994

941

942 Bennington V, Notaro M, Holman KD, 2014: Improving Climate Sensitivity of Deep Lakes  
943 within a Regional Climate Model and Its Impact on Simulated Climate, *J. Climl*, 27, 2886-  
944 2911.

945

946 Bretherton CS, McCaa JR, Grenier H (2004) A new parameterization for shallow cumulus  
947 convection and its application to marine subtropical cloud-topped boundary layers. I.  
948 Description and 1D results. *Mon Weather Rev* 132: 864– 882

949

950 Chan, S. C., E. J. Kendon, H. J. Fowler, S. Blenkinsop, N. M. Roberts, and C. A. T. Ferro,  
951 2014: The value of high- resolution Met Office regional climate models in the simulation  
952 of multi-hourly precipitation extremes. *J. Climate*, 27, 6155–6174,  
953 <https://doi.org/10.1175/JCLI-D-13-00723.1>.

954

955 Chen, Mingyue and Pingping Xie (2008). 'CPC Unified Gauge-based Analysis of Global  
956 Daily Precipitation'. In: *2008 Western Pacific Geophysics Meeting*. ISBN: 0026- 0576.  
957 DOI: [http://dx.doi.org/10.1016/S0026-0576\(07\)80022-5](http://dx.doi.org/10.1016/S0026-0576(07)80022-5).

958

959

960 Clark, P., N. Roberts, H. Lean, S. P. Ballard, and C. Charlton- Perez, 2016: Convection-  
961 permitting models: A step-change in rainfall forecasting. *Meteor. Appl.*, 23, 165–181,  
962 <https://doi.org/10.1002/met.1538>.

963

964 Coppola, E., Sobolowski, S., Pichelli, E. et al. A first-of-its-kind multi-model convection  
965 permitting ensemble for investigating convective phenomena over Europe and the  
966 Mediterranean. *Clim Dyn* 55, 3–34 (2020). <https://doi.org/10.1007/s00382-018-4521-8>

967

968 Coppola E, Giorgi F, Mariotti L, Bi X (2012) RegT-Band: a tropical band version of  
969 RegCM4. *Clim Res* 52: 115–133

970

971 Dacre, H. F., P. A. Clark, O. Martinez-Alvarado, M. A. Stringer, and D. A. Lavers, 2015:  
972 How do atmospheric rivers form? *Bull. Amer. Meteor. Soc.*, 96, 1243-1255,  
973 <https://doi.org/10.1175/BAMS-D-14-00031>.

974 Dale, M., A. Hosking, E. Gill, E. J. Kendon, H. J. Fowler, S. Blenkinsop, and S. C. Chan,  
975 2018: Understanding how changing rainfall may impact on urban drainage systems; les-

976 sons from projects in the UK and USA. *Water Pract. Technol.*, 13, 654–661,  
977 <https://doi.org/10.2166/wpt.2018.069>.

978

979 Diallo, I., Giorgi, F. and Stordal, F. (2018) Influence of Lake Malawi on regional climate  
980 from a double nested regional climate model experiment. *Climate Dynamics*, 50, 3397–  
981 3411. <https://doi.org/10.1007/s00382-017-3811-x>

982

983 Dickinson, R.E., Errico, R.M., Giorgi, F. et al. A regional climate model for the western  
984 United States. *Climatic Change* 15, 383–422 (1989). <https://doi.org/10.1007/BF00240465>

985

986 Dickinson RE, Henderson-Sellers A, Kennedy P (1993) Bio -sphere– atmosphere transfer  
987 scheme (BATS) version 1eas coupled to the NCAR community climate model. TechRep,  
988 National Center for Atmospheric Research TechNote NCAR.TN-387+ STR, NCAR,  
989 Boulder, CO

990

991 Done, J., C. A. Davis, and M. L. Weisman, 2004: The next gener- ation of NWP: Explicit  
992 forecasts of convection using the Weather Research and Forecasting (WRF) model.  
993 *Atmos. Sci. Lett.*, 5, 110–117, <https://doi.org/10.1002/asl.72>.

994

995 Dudhia, J., 1989: Numerical study of convection observed during the winter monsoon  
996 experiment using a mesoscale two-dimensional model. *J. Atmos. Sci.*, 46, 3077–3107.

997

998 Durran D.R. and Klemp J.B.: A compressible model for the simulation of moist mountain  
999 waves, *Mon. Wea. Rev.*, 111, 2341–236, 1983.

1000

1001 Elguindi N., Bi X., Giorgi F. , Nagarajan, B. Pal J., Solmon F., Rauscher S., Zakey S.,  
1002 O'Brien T., Nogherotto R. and Giuliani G., 2017: Regional Climate Model  
1003 RegCMReference ManualVersion 4.7, 49 pp, <https://zenodo.org/record/4603616>

1004

1005 Emanuel KA (1991) A scheme for representing cumulus convection in large-scale  
1006 models. *J Atmos Sci* 48:2313–2335

1007  
1008 Fairall, C.W., E.F. Bradley, J.S. Godfrey, G.A. Wick, J.B. Edson, and G.S. Young, 1996a:  
1009 The cool skin and the warm layer in bulk flux calculations. *J. Geophys. Res.* 101, 1295-  
1010 1308.  
1011  
1012 Fairall, C.W., E.F. Bradley, D.P. Rogers, J.B. Edson, G.S. Young, 1996b: Bulk  
1013 parameterization of air-sea fluxes for TOGA COARE. *J. Geophys. Res.* 101, 3747-3764  
1014  
1015 Funk, C., Peterson, P., Landsfeld, M. et al. The climate hazards infrared precipitation with  
1016 stations—a new environmental record for monitoring extremes. *Sci Data* 2, 150066  
1017 (2015). <https://doi.org/10.1038/sdata.2015.66>  
1018  
1019 Gimeno, L., R. Nieto, M. Vásquez, and D. A. Lavers, 2014: Atmospheric rivers: A mini-  
1020 review. *Front. Earth Sci.*, 2, <https://doi.org/10.3389/feart.2014.00002>.  
1021  
1022 Giorgi F (2019) Thirty years of regional climate modeling: where are we and where are  
1023 we going next? *J Geophys Res Atmos* 124:5696–5723  
1024  
1025 Giorgi F, Coppola E, Solmon F, Mariotti L and others (2012) RegCM4: model description  
1026 and preliminary tests over multiple CORDEX domains. *Clim Res* 52:7-29.  
1027 <https://doi.org/10.3354/cr01018>  
1028  
1029  
1030  
1031 Giorgi F, Francisco R, Pal JS (2003) Effects of a sub-gridscale topography and landuse  
1032 scheme on surface climate and hydrology. I. Effects of temperature and water  
1033 vapor disaggregation. *J Hydrometeorol* 4: 317– 333  
1034  
1035 Giorgi F, Jones C, Asrar G (2009) Addressing climate information needs at the regional  
1036 level: the CORDEX framework. *WMO Bull* 175–183  
1037

1038 Giorgi F, Mearns LO (1999) Introduction to special section: regional climate modeling  
1039 revisited. *J Geophys Res* 104:6335–6352

1040

1041 Giorgi F, Marinucci MR, Bates G (1993a) Development of a second generation regional  
1042 climate model (RegCM2). I. Boundary layer and radiative transfer processes.  
1043 *Mon Weather Rev* 121: 2794–2813

1044

1045 Giorgi F, Marinucci MR, Bates G, DeCanio G (1993b) Development of a second  
1046 generation regional climate model (RegCM2), part II: convective processes and  
1047 assimilation of lateral boundary conditions. *Mon Weather Rev* 121:2814–2832

1048

1049 Giorgi, F., and G. T. Bates, 1989: The Climatological Skill of a Regional Model over  
1050 Complex Terrain. *Mon. Wea. Rev.*, 117, 2325–2347, [https://doi.org/10.1175/1520-0493\(1989\)117<2325:TCSOAR>2.0.CO;2](https://doi.org/10.1175/1520-0493(1989)117<2325:TCSOAR>2.0.CO;2).

1052 G. A. Grell, J. Dudhia and D. R. Stauffer, “A Description of the Fifth Generation Penn  
1053 State/NCAR Mesoscale Model (MM5),” NCAR Tech. Note, NCAR/TN-398+ STR,  
1054 Boulder, 1995, p. 122.

1055

1056 Grell GA (1993) Prognostic evaluation of assumptions used by cumulus  
1057 parameterizations. *Mon Weather Rev* 121: 764– 787

1058

1059 Grell, G., A.J. Dudhia, and D.R. Stauffer, 1994, A description of the fifth-generation Penn  
1060 State/NCAR mesoscale model (MM5). NCAR Technical Note, NCAR/TN- 398+STR.

1061

1062 Gunn, K. L. S., and J. S. Marshall, 1958: The distribution with size of aggregate  
1063 snowflakes. *J. Meteor.*, 15, 452–461, [https://doi.org/10.1175/1520-0469\(1958\)015<0452:TDWSOA>2.0.CO;2](https://doi.org/10.1175/1520-0469(1958)015<0452:TDWSOA>2.0.CO;2).

1065

1066 Gutowski Jr., W. J., Giorgi, F., Timbal, B., Frigon, A., Jacob, D., Kang, H.-S., Raghavan,  
1067 K., Lee, B., Lennard, C., Nikulin, G., O'Rourke, E., Rixen, M., Solman, S., Stephenson,  
1068 T., and Tangang, F.: WCRP COordinated Regional Downscaling EXperiment (CORDEX):

1069 a diagnostic MIP for CMIP6, Geosci. Model Dev., 9, 4087–4095,  
1070 <https://doi.org/10.5194/gmd-9-4087-2016>, 2016

1071

1072 Holtslag A, de Bruijn E, Pan HL (1990) A high resolution air mass transformation model  
1073 for short-range weather fore-casting. *Mon Weather Rev* 118: 1561–1575

1074

1075 Hostetler SW, Bates GT, Giorgi F (1993) Interactive nesting of a lake thermal model within  
1076 a regional climate model for climate change studies. *J Geophys Res* 98: 5045– 5057

1077

1078 Huffman, G. J., and Coauthors, 2007: The TRMM Multisatellite Precipitation Analysis  
1079 (TMPA): Quasi-global, multiyear, combined-sensor precipitation estimates at fine scales.  
1080 *J. Hydrometeor.*, 8, 38–55, doi:<https://doi.org/10.1175/JHM560.1>

1081

1082 Kiehl J, Hack J, Bonan G, Boville B, Breigleb B, WilliamsonD, Rasch P (1996)  
1083 Description of the NCAR Commun -ity Climate Model (CCM3). National Center for  
1084 Atmo spheric Research Tech Note NCAR/TN-420+ STR, NCAR,Boulder, CO

1085

1086 Lean, H. W., P. A. Clark, M. Dixon, N. M. Roberts, A. Fitch, R. Forbes, and C. Halliwell,  
1087 2008: Characteristics of high- resolution versions of the Met Office Unified Model for  
1088 forecasting convection over the United Kingdom. *Mon. Wea. Rev.*, 136, 3408–3424,  
1089 <https://doi.org/10.1175/2008MWR2332.1>.

1090

1091 Lind, P., D. Lindstedt, E. Kjellstrom, and C. Jones, 2016: Spatial and temporal  
1092 characteristics of summer precipitation over central Europe in a suite of high-resolution  
1093 climate models. *J. Climate*, 29, 3501–3518, <https://doi.org/10.1175/JCLI-D-15- 0463.1>.

1094

1095 Hewitt, C. D., and J. A. Lowe, 2018: Toward a European climate prediction system. *Bull.*  
1096 *Amer. Meteor. Soc.*, 99, 1997–2001, <https://doi.org/10.1175/BAMS-D-18-0022.1>.

1097 Hong, S.-Y., H.-M. H. Juang, and Q. Zhao, 1998: Implementation of prognostic cloud  
1098 scheme for a regional spectral model, *Mon. Wea. Rev.*, 126, 2621–2639.

1099

1100 Hong, S.-Y., J. Dudhia, and S.-H. Chen, 2004: A Revised Approach to Ice Microphysical  
1101 Processes for the Bulk Parameterization of Clouds and Precipitation, *Mon. Wea. Rev.*,  
1102 132, 103–120.

1103

1104 Hong, S.-Y., and J.-O. J. Lim, 2006: The WRF Single-Moment 6-Class Microphysics  
1105 Scheme (WSM6), *J. Korean Meteor. Soc.*, 42, 129–151

1106

1107 Hostetler SW, Bates GT, Giorgi F, 1993: Interactive Coupling of Lake Thermal Model with  
1108 a Regional climate Model, *J. Geophys. Res.*, 98(D3), 5045-5057.

1109

1110 Huffman, George J., David T. Bolvin, Eric J. Nelkin, David B. Wolff, Robert F. Adler,  
1111 Guojun Gu, Yang Hong, Kenneth P. Bowman and Erich F. Stocker (2007). *The TRMM*  
1112 *Multisatellite Precipitation Analysis (TMPA): Quasi-Global, Multiyear, Combined-Sensor*  
1113 *Precipitation Estimates at Fine Scales*. DOI: 10.1175/JHM560.1.

1114

1115 Joyce, Robert J., John E. Janowiak, Phillip A. Arkin, Pingping Xie, 2004: CMORPH: A  
1116 Method that Produces Global Precipitation Estimates from Passive Microwave and  
1117 Infrared Data at High Spatial and Temporal Resolution. *J. Hydrometeor*, 5, 487–503

1118

1119 Kain, J. S., 2004: The Kain–Fritsch convective parameterization: An update. *J. Appl.*  
1120 *Meteor.*, 43, 170–181, [https://doi.org/10.1175/1520-0450\(2004\)043<0170:TKCPAU>2.0.CO;2](https://doi.org/10.1175/1520-0450(2004)043<0170:TKCPAU>2.0.CO;2).

1121

1122

1123 Kain, J. S., and J. M. Fritsch, 1990: A one-dimensional entraining/ detraining plume model  
1124 and its application in convective parameterization, *J. Atmos. Sci.*, 47, 2784–2802.

1125

1126 Kendon, E. J., N. M. Roberts, C. A. Senior, and M. J. Roberts, 2012: Realism of rainfall  
1127 in a very high-resolution regional climate model. *J. Climate*, 25, 5791–5806,  
1128 <https://doi.org/10.1175/JCLI-D-11-00562.1>.

1129

1130 Kendon, E. J., and Coauthors, 2017: Do convection-permitting regional climate models  
1131 improve projections of future precipitation change? *Bull. Amer. Meteor. Soc.*, 98, 79–93,  
1132 <https://doi.org/10.1175/BAMS-D-15-0004.1>

1133

1134 Kessler, E., 1969: On the Distribution and Continuity of Water Substance in Atmospheric  
1135 Circulations. *Meteor. Monogr.*, No. 32, Amer. Meteor. Soc., 84 pp.

1136

1137 Khairoutdinov, M. and Kogan, Y.: A new cloud physics parameterization in a large-eddy  
1138 simulation model of marine stratocumulus, *B. Am. Meteorol. Soc.*, 128, 229–243, 2000

1139

1140 Klemp, J.B. and Dudhia, J.: An Upper Gravity-Wave Absorbing Layer for NWP  
1141 Applications, *Monthly Weather Review*, 176, 3987–4004, 2008.

1142

1143 Klemp, J. B. and D. K. Lilly: Numerical simulation of hydrostatic mountain waves, *J.*  
1144 *Atmos. Sci.*, 35, 78–107, 1978.

1145

1146 Lin, Y., Farley, R., and Orville, H.: Bulk parameterization of the snow field in a cloud  
1147 model, *J. Appl. Meteor. Clim.*, 22, 1065–1092, 1983.

1148

1149 Marshall, J. S., and W. McK. Palmer, 1948: The distribution of raindrops with size. *J.*  
1150 *Meteor.*, 5, 165–166.

1151

1152 Matte, Dominic; Laprise, René; Thériault, Julie M.; Lucas-Picher, Philippe (2017). *Spatial*  
1153 *spin-up of fine scales in a regional climate model simulation driven by low-resolution*  
1154 *boundary conditions. Climate Dynamics*, 49(1-2), 563–574. doi:10.1007/s00382-016-  
1155 3358-2

1156

1157 Mlawer, E. J., S. J. Taubman, P. D. Brown, M. J. Iacono, and S. A. Clough, 1997:  
1158 Radiative transfer for inhomogeneous atmospheres: RRTM, a validated correlated-k  
1159 model for the longwave. *J. Geophys. Res.*, 102, 16,663–16,682

1160  
1161 Nogherotto, R., Tompkins, A.M., Giuliani, G., Coppola, E. and Giorgi, F.: Numerical  
1162 framework and performance of the new multiple-phase cloud microphysics scheme in  
1163 RegCM4. 5: precipitation, cloud microphysics, and cloud radiative effects. *Geoscientific*  
1164 *Model Development*, 9(7), 2533-2547, 2016  
1165  
1166 Oleson, K. W., Lawrence, D. M., Bonan, G. B., Drewniak, B., Huang, M., Koven, C. D.,  
1167 Levis, S., Li, F., Riley, W. J., Subin, Z. M., Swenson, S. C., Thornton, P. E., Bozbayik, A.,  
1168 Fisher, R., Kluzeck, E., Lamarque, J. -F., Lawrence, P. J., Leung, L. R., Lipscomb, W.,  
1169 Muszala, S., Ricciuto, D. M., Sacks, W., Sun, Y., Tang, J., and Yang, Z. -L:Technical  
1170 Description of version 4.5 of the Community Land Model (CLM),Ncar Technical Note  
1171 NCAR/TN-503+STR, National Center for Atmospheric Research, Boulder, CO, 422 pp,  
1172 DOI: 10.5065/D6RR1W7M, 2013.  
1173  
1174 Pal JS, Small E, Eltahir E (2000) Simulation of regional-scale water and energy budgets:  
1175 representation of subgrid cloud and precipitation processes within RegCM. *J Geo-phys*  
1176 *Res* 105: 29579–29594  
1177  
1178 Pal JS et al (2007) The ICTP RegCM3 and RegCNET: regional climate modeling for the  
1179 developing world. *Bull Am Meteorol Soc* 88:1395–1409  
1180  
1181 Pichelli, E., Coppola, E., Sobolowski, S. *et al.* The first multi-model ensemble of regional  
1182 climate simulations at kilometer-scale resolution part 2: historical and future simulations  
1183 of precipitation. *Clim Dyn* (2021). <https://doi.org/10.1007/s00382-021-05657-4>  
1184  
1185 Prein, Andreas F. and Andreas Gobiet (2017). 'Impacts of uncertainties in European  
1186 gridded precipitation observations on regional climate analysis'. In: *International Journal*  
1187 *of Climatology*. ISSN: 10970088. DOI: 10.1002/joc.4706  
1188  
1189 Prein, A. F. *et al.* A review on regional convection-permitting climate modeling:  
1190 demonstrations, prospects, and challenges. *Rev. Geophys.* 53, 323–361 (2015).

1191  
1192 Ralph, F. M., P. J. Neiman, G. A. Wick, S. I. Gutman, M. D. Dettinger, D. R. Cayan, and A.  
1193 B. White, 2006: Flooding on California's Russian River: Role of atmospheric rivers.  
1194 *Geophys. Res. Lett.*, 33, L13801, <https://doi.org/10.1029/2006GL026689>  
1195  
1196 Ralph, F. M., M. D. Dettinger, M. M. Cairns, T. J. Galarneau, and J. Eylander, 2018:  
1197 Defining "atmospheric river": How the Glossary of Meteorology helped resolve a debate.  
1198 *Bull. Amer. Meteor. Soc.*, 99, 837–839, <https://doi.org/10.1175/BAMS-D-17-0157.1>  
1199  
1200 Rutledge, S. A., and P. V. Hobbs, 1983: The mesoscale and microscale structure and  
1201 organization of clouds and precipitation in midlatitude cyclones. Part VIII: A model for the  
1202 "seeder-feeder" process in warm-frontal rainbands. *J. Atmos. Sci.*, 40, 1185–1206.  
1203  
1204 Skamarock WC, Klemp JB, Dudhia J, Gill DO, Barker DM, Duda MG, Huang XY, Wang  
1205 W, Powers JG. 2008. 'A description of the advanced research WRF version 3', Technical  
1206 Note NCAR/TN-475+STR. NCAR: Boulder, CO  
1207  
1208 Schwartz, C. S., 2014: Reproducing the September 2013 record- breaking rainfall over  
1209 the Colorado Front Range with high- resolution WRF forecasts. *Wea. Forecasting*, 29,  
1210 393–402, <https://doi.org/10.1175/WAF-D-13-00136.1>  
1211  
1212 Sitz, L. E., F. Sante, R. Farneti, R. Fuentes-Franco, E. Coppola, L. Mariotti, M. Reale, et  
1213 al. 2017. "Description and Evaluation of the Earth System Regional Climate Model  
1214 (RegCM-ES)." *Journal of Advances in Modeling Earth Systems*.  
1215 doi:10.1002/2017MS000933  
1216  
1217 Song Y, Semazzi HMF, Xie L, Ogallo LJ, 2004: A coupled regional climate model for the  
1218 Lake Victoria Basin of East Africa. *Int. J. Climatol.* 24: 57–75.  
1219

1220 Sun X, Xie L, Semazzi F, Liu B, 2015: Effect of Lake Surface Temperature on the Spatial  
1221 Distribution and Intensity of the Precipitation over the Lake Victoria Basin. *Mon. Wea.  
1222 Rev.* 143: 1179-1192.

1223

1224 Sundqvist, H., Berge, E., and Kristjansson, J.: Condensation and cloud parameterization  
1225 studies with a mesoscale numerical weather prediction model, *Mon. Weather Rev.*, 117,  
1226 1641-1657, 1989.

1227

1228 Talling, J. F. (1969) The incidence of vertical mixing, and some biological and chemical  
1229 consequences, in tropical African lakes, *Verh. Int. Ver. Limnol.* 17, 998-1012 DOI:  
1230 10.1080/03680770.1968.11895946

1231

1232 Tiedtke, M., 1989, A comprehensive mass flux scheme for cumulus parametrization in  
1233 large-scale models. *Mon. Weather Rev.*, 117, 1779-1800

1234

1235 Tiedtke, M., 1993: Representation of Clouds in Large-Scale Models. *Mon. Wea. Rev.*,  
1236 121, 3040-3061, [https://doi.org/10.1175/1520-0493\(1993\)121<3040:ROCILS>2.0.CO;2](https://doi.org/10.1175/1520-0493(1993)121<3040:ROCILS>2.0.CO;2)

1237

1238 Tiedtke, M., . 1996: An extension of cloud-radiation parameterization in the ECMWF  
1239 model: The representation of subgrid-scale variations of optical depth. *Mon. Wea. Rev.*,  
1240 124, 745-750

1241

1242 Tompkins, A.: Ice supersaturation in the ECMWF integrated fore-cast system, *Q. J. Roy.  
1243 Meteor. Soc.*, 133, 53-63, 2007

1244

1245 Tripoli, G. J., and W. R. Cotton, 1980: A numerical investigation of several factors  
1246 contributing to the observed variable intensity of deep convection over south Florida. *J.  
1247 Appl. Meteor.*, 19, 1037-1063.

1248

1249 Williams PD. 2009. A proposed modification to the Robert-Asselin time filter. *Mon.  
1250 Weather Rev.* 137: 2538-2546

1251

1252 Weisman, M. L., C. Davis, W. Wang, K. W. Manning, and J. B. Klemp, 2008: Experiences  
1253 with 0–36-h explicit convective forecasts with the WRF-ARW model. *Wea. Forecasting*,  
1254 23, 407–437, <https://doi.org/10.1175/2007WAF2007005.1>.

1255

1256 Weusthoff, T., F. Ament, M. Arpagaus, and M. W. Rotach, 2010: Assessing the benefits  
1257 of convection-permitting models by neighborhood verification: Examples from MAP D-  
1258 PHASE. *Mon. Wea. Rev.*, 138, 3418–3433, <https://doi.org/10.1175/2010MWR3380.1>.

1259

1260 Zeng X, Zhao M, Dickinson RE (1998) Intercomparison of bulk aerodynamic algorithms  
1261 for the computation of sea surface fluxes using TOGA COARE and TAO data. *J Clim* 11:  
1262 2628–2644

1263

1264 Zhu, Y., and R. E. Newell, 1998: A proposed algorithm for moisture fluxes from  
1265 atmospheric rivers. *Mon. Wea. Rev.*, 126, 725–735, [https://doi.org/10.1175/1520-0493\(1998\)126<0725:APAFMF>2.0.CO;2](https://doi.org/10.1175/1520-0493(1998)126<0725:APAFMF>2.0.CO;2).